1992-12

Errors caused by incompatible wind and buoyancy forcing in the ocean general circulation models.

Kuo, Yu-Heng

Monterey, California. Naval Postgraduate School

NAVAL POSTGRADUATE SCHOOL
Monterey, California

THESIS

ERRORS CAUSED BY INCOMPATIBLE WIND AND BUOYANCY FORCING IN THE OCEAN GENERAL CIRCULATION MODELS

by

Kuo, Yu-Heng

December 1992

Thesis Advisor: Peter C. Chu
Co-Advisor: Robert L. Haney

UNCLASSIFIED

SECURITY CLASSIFICATION OF THIS PAGE

REPORT DOCUMENTATION PAGE

1a. REPORT SECURITY CLASSIFICATION Unclassified	1b. RESTRICTIVE MARKINGS
2a. SECURITY CLASSIFICATION AUTHORITY	3. DISTRIBUTION/AVAILABILITY OF REPORT
2b. DECLASSIFICATION/DOWNGRADING SCHEDULE	Approved for public release; distribution is unlimited.
4. PERFORMING ORGANIZATION REPORT NUMBER(S)	5. MONITORING ORGANIZATION REPORT NUMBER(S)
6a. NAME OF PERFORMING ORGANIZATION Naval Postgraduate School 6b. OFFICE SYMBOL (*If applicable*) MR	7a. NAME OF MONITORING ORGANIZATION Naval Postgraduate School
6c. ADDRESS (*City, State, and ZIP Code*) Monterey, CA 93943-5000	7b. ADDRESS (*City, State, and ZIP Code*) Monterey, CA 93943-5000
8a. NAME OF FUNDING/SPONSORING ORGANIZATION 8b. OFFICE SYMBOL (*If applicable*)	9. PROCUREMENT INSTRUMENT IDENTIFICATION NUMBER
8c. ADDRESS (*City, State, and ZIP Code*)	10. SOURCE OF FUNDING NUMBERS Program Element No. / Project No. / Task No. / Work Unit Accession Number

11. TITLE (*Include Security Classification*)
ERRORS CAUSED BY INCOMPATIBLE WIND AND BUOYANCY FORCING IN THE OCEAN GENERAL CIRCULATION MODELS

12. PERSONAL AUTHOR(S)
Kuo, Yu-Heng

13a. TYPE OF REPORT	13b. TIME COVERED	14. DATE OF REPORT (*year, month, day*)	15. PAGE COUNT
Master's Thesis	From To	December 1992	73

16. SUPPLEMENTARY NOTATION
The views expressed in this thesis are those of the author and do not reflect the official policy or position of the Department of Defense or the U.S. Government.

17. COSATI CODES			18. SUBJECT TERMS (*continue on reverse if necessary and identify by block number*)
FIELD	GROUP	SUBGROUP	Wind Forcing, Buoyancy Forcing, Ekman transport, GFDL MOM, Surface Thermal Boundary Conditions

19. ABSTRACT (*continue on reverse if necessary and identify by block number*)

The Geophysical Fluid Dynamics Laboratory Modular Ocean Model (GFDL MOM) is used to investigate the model difference between compatible and incompatible surface wind and buoyancy forcing. The atmosphere is a physical system in which surface wind and temperature fields are related, however in most ocean numerical models, the wind stress and buoyancy forcing are usually specified separately, i.e., no constraint between the surface wind stress and surface air temperature is considered. In reality, only one of these two fields can be prescribed in the atmosphere-driven ocean models. When the surface wind field is prescribed, the surface air temperature should be derived, and vice versa. If the two related fields are treated as totally independent in forcing the ocean models the results will be distorted. Since the model solutions depend upon the atmospheric forcing, it is important that we study the compatibility between the wind and buoyancy forcings and the effect which incompatibility might have on the ocean numerical models.

This study shows that the surface wind and buoyancy forcing widely used in ocean numerical models are incompatible. Such an incompatibility results in 21% error in the total northward transport of heat, 16% error in the total northward transport of salt, 25% error in v velocity, and 16% error in w velocity.

20. DISTRIBUTION/AVAILABILITY OF ABSTRACT	21. ABSTRACT SECURITY CLASSIFICATION	
☒ CLASSIFIED/UNLIMITED ☐ SAME AS REPORT ☐ DTIC USERS	UNCLASSIFIED	
22a. NAME OF RESPONSIBLE INDIVIDUAL Peter C. Chu	22b. TELEPHONE (*Include Area code*) (408)646-3257	22c. OFFICE SYMBOL OC/Cu

DD FORM 1473, 84 MAR — 83 APR edition may be used until exhausted. All other editions are obsolete.

SECURITY CLASSIFICATION OF THIS PAGE
Unclassified

Approved for public release; distribution is unlimited.

ERRORS CAUSED BY INCOMPATIBLE WIND AND BUOYANCY FORCING IN THE OCEAN GENERAL CIRCULATION MODELS

by

Kuo, Yu-Heng
Lieutenant, Taiwan, R.O.C. Navy
B.S., Chinese Naval Academy, 1984

Submitted in partial fulfillment
of the requirements for the degree of

MASTER OF SCIENCE IN METEOROLOGY

from the
NAVAL POSTGRADUATE SCHOOL

December 1992

ABSTRACT

The Geophysical Fluid Dynamics Laboratory Modular Ocean Model (GFDL MOM) is used to investigate the model difference between compatible and incompatible surface wind and buoyancy forcing. The atmosphere is a physical system in which surface wind and temperature fields are related, however in most ocean numerical models, the wind stress and buoyancy forcing are usually specified separately, i.e., no constraint between the surface wind stress and surface air temperature is considered. In reality, only one of these two fields can be prescribed in the atmosphere-driven ocean models. When the surface wind field is prescribed, the surface air temperature should be derived, and vice versa. If the two related fields are treated as totally independent in forcing the ocean models the results will be distorted. Since the model solutions depend upon the atmospheric forcing, it is important that we study the compatibility between the wind and buoyancy forcings and the effect which incompatibility might have on the ocean numerical models.

This study shows that the surface wind and buoyancy forcing widely used in ocean numerical models are incompatible. Such an incompatibility results in 21% error in the total northward transport of heat, 16% error in the total northward transport of salt, 25% error in v velocity, and 16% error in w velocity.

TABLE OF CONTENTS

LIST OF FIGURES

I. INTRODUCTION

In the atmosphere the surface wind and the sea surface air temperature (SSAT) are closely related. As such, thermal field and the surface wind field cannot be prescribed independently in a numerical model.

However, in current ocean numerical models, the surface wind and the net surface heat flux are usually prescribed independently. The assumption that the prescribed surface wind field always matches the surface thermal field (or the net surface heat flux) is rather unrealistic. Contrary to the assumption, the two fields do not match each other in many cases. The imbalance between the surface wind and the surface thermal field gives rise to certain adjustment processes, thus changing the original forcing field. Consequently, during the entire integration of the ocean numerical models these two forcing fields will not maintain the prescribed form.

That there is an obvious incompatibility can be found from the pioneering work by Takano (1975), which states that the SSAT is a function of latitude (y) only, and that the surface wind stress is a function of position (x,y) and season (t)

$$T_a = T_a(y), \quad u_s = u_s(x,y,t), \quad v_s = v_s(x,y,t) \qquad (1)$$

In equation (1) the atmospheric surface isotherms are given by straight lines running parallel to the x-axis. However, surface winds have both x and y components and seasonal variation. It is thus unlikely that the atmospheric surface isotherms would

remain linear and in a steady-state when there are surface winds blowing across the isotherms.

Haney (1971) states that by employing a heat budget analysis appropriate to zonally and time averaged conditions within the atmosphere, it can be shown that the net downward heat flux Q at the ocean's surface is expressed as

$$Q = Q_2 (T_A - T_s) \tag{2}$$

where T_A is an apparent atmospheric equilibrium temperature, T_s is the sea surface temperature, and Q_2 is a coefficient determined from the zonally and time average data. The zonally averaged surface zonal winds and apparent air temperature were broadly used as mechanical and thermal forcing in ocean numerical models when the surface thermal boundary conditions (2) in Haney (1971) are met. This approach is well accepted by ocean modelers.

Several combinations of surface wind stress τ and T_A in ocean models are listed as follows (Chu, 1992). In Davey (1983) model, the atmospheric temperature T_A is specified by

$$T_A(y) = \begin{cases} T_s & , \quad y < y_s \\ T_s + \dfrac{(T_N - T_s)}{2}\left[1 - \cos\dfrac{\pi (y - y_s)}{l}\right] & , \quad y_s < y < y_s + l \\ T_N & , \quad y_s + l < y \end{cases} \tag{3}$$

with l = 2000 km, T_s = 12°C, and T_N = 8°C. The surface winds are set to zero, thus

$$(u_s,\ v_s) = 0 \qquad (4)$$

The important question arises as to whether the atmospheric forcing indicated by (3) and (4) can last 2000 days, the period over which the model was integrated. Geostrophic baroclinic zonal atmospheric flow is usually driven by the north-south SSAT gradient while the cross isothermal surface winds is generated by the resulting friction. Hence, the atmospheric mechanical forcing given by (4) is not consistent with the atmospheric thermal forcing of (3).

There are other renowned ocean model, such as Robinson et al (1977), Semtner and Mintz (1977), Cox and Bryan (1984), Cox (1985), Huang (1989), and Willmott and Darby (1990). In general, the wind stress is purely zonal ($\tau_y = 0$) and assumed as a sinusoidal function (or other form) of y. T_A is assumed as a linear function of y, e.g., in Robinson el al (1977),

$$\tau_x = \tau_0 \cos\pi \frac{y - y_N}{y_N - y_S}, \quad \tau_y = 0, \quad T_A = 26 - \frac{7}{9}(y - y_s) \qquad (5)$$

Since the ocean numerical models are generally integrated over long time interval, such as 880 years in Bryan and Cox (1984), it is important to determine whether or not the surface wind and the SSAT as employed by the ocean numerical models are consistent. Where there are inconsistency, the effect of the inconsistency on the ocean circulation should be further investigated.

The main purpose of this study is to address these differences. For this, experimentations with a three-dimensional primitive equation ocean model are performed.

Through model simulation of the principal aspects of the Pacific Ocean, we gain a better understanding of the differences between the atmospheric parameters representing mechanical and buoyancy forcing, i.e., the surface wind and SSAT field.

A statement of the problem in existing ocean numerical models is contained in this chapter. Chapter II gives a description of the Modular Ocean Model (MOM). Chapter III describes the compatibility between surface wind stress and buoyancy forcing. Chapter IV shows the errors caused by incompatible forcing. Finally, Chapter V states the conclusions.

II. DESCRIPTION OF THE MODULAR OCEAN MODEL (MOM)

A. INTRODUCTION

More than two decades have passed since the first 3-dimensional primitive equation numerical ocean model was used to study the most basic aspects of large-scale, baroclinic ocean circulation (Bryan and Cox, 1967). A description of the physics and numerics involved was published in Bryan (1969). In this model, the prediction of currents is carried out using the Navier-Stokes equations with three basic assumptions. The Boussinesq approximation is adopted, in which density differences are neglected except in the buoyancy term. The hydrostatic assumption is made in which local acceleration and other terms of equal order are eliminated from the equation of vertical motion. Lastly, closure is attained by adopting the turbulent viscosity hypothesis in which stresses exerted by scales of motion too small to be resolved by the grid are represented as an enhanced molecular mixing. The temperature and salinity are calculated using conservation equations, again utilizing a turbulent mixing hypothesis for closure. The equations are linked by a simplified equation of state.

For the purpose of computational efficiency several techniques are used. High speed, external gravity waves are eliminated by the "rigid-lid" approximation, and a Laplacian equation is solved for the non-divergent, vertically averaged flow. The timestep limitation, i.e., the half pendulum day constraint associated with inertia-gravity waves, is overcome by a semi-implicit treatment of the Coriolis term.

Considerable improvement was made to the structure of the FORTRAN code of this model by Semtner (1974) who, at the same time, added various features to the mathematical formulation, chief of which was the use of "hole relaxation" (Takano, 1974) in the solution of the external mode for a model with islands. This version of the model has been adopted by many investigators and has seen considerable use for a number of years in the ocean modelling work at GFDL. During this time, as vector processing machines became more demanding of suitable FORTRAN structure, significant changes have been made to the code for efficiency purposes. It has also been generalized in several ways, among which is the incorporation of variable grid spacing in the horizontal, and an arbitrary number of tracer prognostic variables. The relaxation code for the solution of the external mode has been redesigned, and a better technique for establishing the initial guess has reduced the scans-to-convergence considerably.

Two objectives have been sought in designing the code for use outside of GFDL. First, it has been made universal to some degree, by the use of optional code lines. A separate, FORTRAN coded updating utility is provided to carry out these operations.

B. THE MODEL DESCRIPTION

The GFDL Modular Ocean Model (acronym MOM) version 1.0...Dec 1, 1990 is a three dimensional primitive equation general ocean circulation model intended for use as a flexible tool for exploring ocean and coupled air-sea applications over a wide range of space and time scales.

MOM has been written as a collaborative effort by Ron Pacanowski, Keith Dixon, and Anthony Rosati at the National Oceanographic and Atmospheric Administration's Geophysical Fluid Dynamics Laboratory in Princeton, New Jersey. It is the successor to the code written by Michael Cox, documented in the GFDL Ocean Tech Report #1, (1984). As was the case for the Cox model and the Semtner model (UCLA Dept. of Meteorology Tech. Report No. 9, 1974) that preceded it, MOM is a Fortran implementation of equations described by Kirk Bryan (1969).

For my investigation, I use the Pacific Ocean as the region of interest in the MOM model. The region is defined by 160° of longitude from 120°E to 280°E and extending from 60°S to 60°N. A constant depth of 5700 m is assumed. The horizontal resolution is 5° in longitude and 5° in latitude. There are 15 levels in the vertical, with resolution varying from 30 m near the surface to 836 m near the bottom.

The time manager clock parameters for setting time of model initial conditions are year0 = starting year (set to be 0), month0 = starting month (set to be 1), and day0 = starting day (set to be 1). Using logical Julian calendar in MOM model, the time period of integrations is 60 years. The time step for both barotropic and baroclinic velocity is 1 hour. For density and tracers (potential temperature and salinity), the time step is 1 day.

The MOM model uses an efficient grid system. Horizontally, tracer quantities are defined at the centers of "t" grid boxes and velocities are defined at the centers of "u,v" grid boxes. The centers of "u,v" grid boxes are located at the northeast corners of "t" grid boxes. The first "t" grid box is located in the southwest corner of the "t" grid.

This grid system is replicated and stacked vertically one on top of another from the surface of the ocean downward. Vertically, tracers and velocities are defined at the centers of their corresponding boxes and are set at the same depths.

The values for the mixing coefficients of MOM model were chosen as 10^9 cm^2/s and 1 cm^2/s for the horizontal and vertical viscosity, respectively, and 2×10^7 cm^2/s and 20 cm^2/s for the horizontal and vertical diffusivity, respectively. The bottom drag coefficient was set to 0.

C. BASIC EQUATIONS OF MOM MODEL

The basic equations of the model are written here in continuous form.

Let

$$\begin{aligned} m &= \sec\phi \\ n &= \sin\phi \\ f &= 2\Omega\sin\phi \end{aligned} \tag{6}$$

where ϕ is latitude.

An advective operator,

$$\Gamma(\mu) = m\frac{1}{a}\left[(u\mu)_\lambda + \left(v\mu\frac{1}{m}\right)_\phi\right] + (w\mu)_z \tag{7}$$

is adopted in which μ is any scalar quantity, λ is longitude and a is the radius of the earth.

The equations of motion are then

$$u_t + \Gamma(u) - fv = -m\frac{1}{a}\left(\frac{p}{\rho_0}\right)_\lambda + F^u \tag{8}$$

$$v_t + \Gamma(v) + fu = -\frac{1}{a}\left(\frac{p}{\rho_0}\right)_\phi + F^v \tag{9}$$

where ρ_0 is taken to be unity.

The local pressure, p, is given by the hydrostatic relation,

$$p(z) = p^s + \int_z^0 g\rho\, dz \tag{10}$$

where p^s is the pressure at the surface of the ocean.

The continuity equation is

$$\Gamma(1) = 0 \tag{11}$$

The conservation equation,

$$T_t + \Gamma(T) = F^T \tag{12}$$

applies to any "tracer" type of quantity carried in the model. These include the active tracers, potential temperature and salinity (active in the sense that they appear in the equation of state), and any passive tracers such as Carbon 14 or Tritium.

The equation of state is

$$\rho = \rho(\theta, S, z) \tag{13}$$

where θ is potential temperature, S is salinity and the depth dependence arises from compression effects. In the present model, (13) is represented by a polynomial fit to the Knudsen formula (Bryan and Cox, 1972).

Let

$$\nabla^2\mu = m^2\mu_{\lambda\lambda} + m\left(\frac{\mu_\phi}{m}\right)_\phi \tag{14}$$

The effects of turbulent mixing are

$$F^u = A_{MV}u_{zz} + A_{MH}a^{-2}[\nabla^2 u + (1 - m^2n^2)u - 2nm^2v_\lambda] \tag{15}$$

$$F^v = A_{MV}v_{zz} + A_{MH}a^{-2}[\nabla^2 v + (1 - m^2n^2)v + 2nm^2u_\lambda] \tag{16}$$

$$F^T = \left[\left(\frac{A_{TV}}{\delta}\right)T_z\right]_z + A_{TH}a^{-2}\nabla^2 T \tag{17}$$

where A is the mixing coefficient corresponding to M (momentum), T (tracer), V (vertical), and H (horizontal).

In nature, vertical mixing is known to be a rather complex function of vertical stability. Since this process is still not well understood, we have adopted a simple, uniform mixing under statically stable conditions, and an infinite mixing under statically unstable conditions. This is done by specifying δ to be

$$\delta = \begin{cases} 1 & \dfrac{\partial^2\rho}{\partial z^2} < 0 \\ 0 & \dfrac{\partial^2\rho}{\partial z^2} > 0 \end{cases} \tag{18}$$

At lateral walls, the boundary conditions are

$$u,\ v,\ T_n = 0 \tag{19}$$

where the n subscript indicates a local derivative with respect to the coordinate normal to the wall. At the surface,

$$\begin{cases} \rho_0 A_{MV}(u_z,\ v_z) = (\tau^\lambda,\ \tau^\phi) \\ A_{TV}(T_z) = \eta \\ w = 0 \end{cases} \tag{20}$$

The "rigid-lid" assumption of zero vertical motion at the surface filters out high speed external gravity waves which would otherwise seriously limit the length of the time step used in the numerical integration. The quantities τ^λ, τ^ϕ are the zonal and meridional components of the specified surface stress, and η is a flux through the surface, of the particular tracer involved.

At the bottom,

$$\begin{cases} \rho_0 A_{MV}(u_z,\ v_z) = 0 \\ \Gamma_z = 0 \\ w = -mua^{-1}H_\lambda - va^{-1}H_\phi \end{cases} \tag{21}$$

Combining (8) and (9) with (10), we derive

$$\begin{cases} u_t = u_t' - ma^{-1}p_\lambda^s \\ v_t = v_t' - a^{-1}p_\phi^s \end{cases} \tag{22}$$

where

$$u_t' = -\Gamma(u) + fv - mga^{-1}\int_z^0 \rho_\lambda dz' + F^u \tag{23}$$

$$v_t' = -\Gamma(v) - fu - a^{-1}\int_z^0 \rho_\phi dz' + F^v \tag{24}$$

Let us define

$$u = \hat{u} + \overline{u}; \qquad v = \hat{v} + \overline{v} \tag{25}$$

where

$$\overline{\mu} = H^{-1}\int_{-H}^0 \mu dz \tag{26}$$

Then, since p^s is not a function of depth,

$$\hat{u}_t = u_t' - \overline{u_t'}; \qquad \hat{v}_t = v_t' - \overline{v_t'} \tag{27}$$

Since all terms on the right of (23) and (24) are known, (27) may be solved for the internal modes of momentum. Under the rigid-lid boundary condition, the external mode of momentum may be represented by a volume transport stream function, ψ,

$$\overline{u} = -(aH)^{-1}\psi_\phi; \qquad \overline{v} = m(aH)^{-1}\psi_\lambda \tag{28}$$

This is shown by integrating (11) vertically, substituting (28) and noting that the boundary conditions (20) and (21) on w are satisfied. A prognostic equation for ψ may be obtained by averaging (22) vertically, and eliminating terms in p^s by applying the curl operator,

$$curl_z(\overline{v}_t,\ \overline{u}_t) = ma^{-1}\left[\overline{v}_{t\lambda} - \left(\frac{\overline{u}}{m}\right)_{t\phi}\right] \tag{29}$$

Substituting (28),

$$\left[\frac{m\psi_{t\lambda}}{Ha^2}\right]_\lambda + \left[\frac{\psi_{t\phi}}{mHa^2}\right]_\phi = a^{-1}\left[\overline{v'_{t\lambda}} - \left(\frac{\overline{u'_t}}{m}\right)_\phi\right] \tag{30}$$

The boundary condition on ψ at lateral walls, corresponding to (19) is

$$\psi_\phi = \psi_\lambda = 0 \tag{31}$$

This condition is satisfied by setting ψ constant over each unconnected land mass comprising the ocean boundary. In the case of an enclosed basin with no islands, ψ may be set to zero over the boundary forming land mass. If, in addition, islands are present, the associated constant for each island reflects the net flow around the island and must therefore be predicted by the governing equations. The method used is "hole relaxation" in which the line integral of the quantity ∇p^s, taken around the island, is required to vanish. Averaging (22) vertically, integrating around the coast of the island and setting the contribution due to p^s to zero, the predictive equation,

$$\oint\left\{\left[\frac{m\psi_{t\lambda}}{H}\right]d\phi - \left[\frac{\psi_{t\phi}}{mH}\right]d\lambda\right\} = a\oint\left[\overline{v'_t}d\phi + \left(\frac{\overline{u'_t}}{m}\right)d\lambda\right] \tag{32}$$

is obtained. Applying the Stokes theorem yields a more useful form,

$$a^{-2}\int_A\left\{\left[\frac{m\psi_{t\lambda}}{H}\right]_\lambda + \left[\frac{\psi_{t\phi}}{mH}\right]_\phi\right\}dA = a^{-1}\int_A\left[\overline{v'_{t\lambda}} - \left(\frac{\overline{u'_t}}{m}\right)_\phi\right]dA \tag{33}$$

Note that (33) is simply an area integral of (30), taken over the island.

D. PROGRAM FLOW OF MOM MODEL

The FORTRAN code of the model consists of the main program OCEAN, and seven subroutines. Their functions are described below.

OCEAN: Performs all operations. This is done only once at the beginning of each run of the model. The program calls STEP once per timestep, and attends to operations which must be done at the end of each run.

STEP: Called once per timestep by OCEAN, it initializes various quantities, bootstraps the row-by-row computation of prognostic variables, manages the I/O for the latter, and performs various analysis procedures on the progressing solution.

CLINIC: Called once per row by STEP, it computes the internal mode component of the u and v velocities as well as the vorticity driving function for use by RELAX later in determining the external mode.

TRACER: Called once per row by STEP, it computes temperature, salinity, and any tracers which are carried in the model.

RELAX: Called once at the end of each timestep by STEP, it takes the vorticity driving function computed in CLINIC and, using sequential overralaxation, solves the Laplacian equation for the external mode of velocity in terms of a mass transport stream function.

STATE: Called by CLINIC and TRACER once per row, and STEP in the bootstrap procedure, it computes normalized densities by using a third order polynomial fit to the Knudsen formula.

MATRIX: Called by STEP on specified timesteps, it is a general 2-dimensional array printing routine.

ODAM: (Ocean Direct Access Manager)

Used primarily by STEP, it is a set of routines which is responsible for handling the transfer of data between memory and disc (virtual disc residing in memory in the core contained mode).

In summary, for one timestep, OCEAN calls STEP, which establishes the proper data in memory and calls CLINIC and TRACER row-by-row from south to north through the basin. Upon completing the final row, STEP calls RELAX and returns control to OCEAN, which may call STEP for another timestep.

Two additional subroutines, FINDEX and FILTER are used when Fourier filtering is needed to overcome the timestep limitation arising from convergence of meridians at high latitudes.

E. DISC I/O SYSTEM

Next to the equations themselves, the component of the code which accounts for the greatest complexity is the I/O system. The purpose of this system is twofold. First, having a complete record of all prognostic variables on permanent disc at the end of each timestep allows restarting an experiment from an earlier run, or from a machine malfunction. Secondly, during a run, it is generally impossible to fit the three dimensional arrays in memory entirely. The I/O system is designed to feed data to and from memory in a row-by-row manner. Data for one row, including all east-west and

vertical grid points is termed a "slab". At any one time, only the slabs necessary for the computation are present. While the computation for one row proceeds, the I/O system is feeding the slab just computed, back to disc and fetching the slab which will be needed to compute the next row. If the disc transfers are done fast enough, no wait for data will be needed at the beginning of each row and the system is said to be completely "buffered".

Three disc units are needed for the process when using centered differencing in time; one for the N timestep data (read), one for the N-1 timestep data (read), and one for the newly computed N+1 timestep data (written). Since the N level on one timestep becomes the N-1 level for the next, it is convenient to permute the disc units to minimize data transfers. Thus, on timestep 1, N-1 and N data are read from units 13 and 14, and the N+1 data is written to 15. On timestep 2, units 14 and 15 are read and the N+1 data is written to 13. On timestep 3, 15 and 13 are read with the N+1 data going to 14, etc.

Possibly the most abstruse feature of the model is the manner in which the "slab incidental data" is handled. Just as the slab system reduces the row dimension of the 3-dimensional prognostic variables to 3, it can also be used to reduce the row dimension of 2-dimensional variables which would otherwise add considerably to the memory requirements. Also, if these variables are constant in time, there is no need to keep multiple time records of them. Consider two arrays, A and B, for which there is data, invariant in time, at each row and column horizontally across the grid. They may be carried in the model as "slab incidental data", thereby reducing their row dimension to

3. Furthermore, let A reside in the slab corresponding to the N-1 time level of the primary slab data, and B reside in the N level slab. The diagram below illustrates the 6 timestep cycle which the permuting disc units execute, with N-1, N and N+1 denoting the primary slab data, and A, B denoting slab incidental data.

TIMESTEP:	1	2	3	4	5	6	7
UNIT							
13	N-1,A	N+1,B	N,B	N-1,B	N+1,A	N,A	N-1,A
14	N,B	N-1,B	N+1,A	N,A	N-1,A	N+1,B	N,B
15	N+1,A	N,A	N-1,A	N+1,B	N,B	N-1,B	N+1,A

Note that on even timesteps, the slab incidental data enters memory in the wrong slabs and must be switched between slabs N and N-1. Also, storing of A and B into the N+1, slab must be alternated on successive timesteps. In the base code, FKMU and WSY are "A" type arrays, and FKMT and WSX are "B" type arrays.

Disc unit 12 is used primarily for the storage of 2-dimensional, horizontal fields. It is divided into 7+ blocks in the following manner:

Blocks 1-3: permuting blocks for the stream function at N-1, N, and N+1 time levels

Block 4: reciprocal of total depth

Blocks 5-6: permuting blocks for former relaxation solutions

Block 7+: start and end indices (additional blocks are added as necessary when filtering indices fill block 7)

Finally, unit 11 contains the timestep counter, total elapsed time, and the area and volume of the basin.

Data is fed to and from these units by means of the entry points of subroutine ODAM. It, in turn, must use a direct access I/O package provided locally. If FORTRAN direct access I/O is available, with a facility to buffer the operations (such as a FIND statement), the QDAM calls in ODAM of the base code may be replaced by the appropriate FORTRAN statements. Otherwise, a specially written set of I/O utilities such as QDAM must be supplied. If, instead, the core-contained option is invoked, no such package in needed.

III. COMPATIBILITY BETWEEN SURFACE WIND STRESS AND BUOYANCY FORCING

Wind stress and buoyancy forcing are independently designated in most ocean models, e.g., no constraint has been considered between the surface wind stress and surface air temperature (or net surface heat flux). The atmosphere actually is a unified physical system. For atmospheric motion on the scale of the ocean basin considered here, the wind and temperature fields are related to each other through the thermal wind relation. Only one of the two (either wind or air temperature) can be prescribed in the atmosphere-driven ocean models. Thus, treating the 2 fields as totally independent will produce physically unrealistic atmospheric forcing in the ocean models. This gives rise to a distortion of model results since the solutions largely depend upon the atmospheric forcing. Therefore, it is important to study the compatibility between the wind and buoyancy forcing and the effect of incompatibility on the model results before running any ocean numerical model.

In many ocean models (e.g., Davis, 1983, Robinson et al. 1977, etc.) the SSAT is assumed zonal symmetric. Therefore, if the surface wind (u_s^*, v_s^*) and SSAT fields used in ocean models are compatible then they can be denoted by combinations of sinusoidal functions (Chu, 1992), i.e.,

$$u_{s*} = U_T \sum_n u_{sn} \sin k_n \pi y \qquad (34)$$

$$v_{s*} = U_T \sum_n v_{sn} \sin k_n \pi y \tag{35}$$

$$\theta_{s*} = (\Delta T) \sum_n \theta_{sn} \cos k_n \pi y \tag{36}$$

where the subscript '*' indicates the dimensional variables, k_n (n = 1, 2,...) are not necessary integers. It should be noted that (u_s^*, v_s^*) is the total surface wind, i.e.,

$$u_{s*} = u_{G*} + u_*, \quad v_{s*} = v_*, \quad at\ z = 0 \tag{37}$$

Since the flow variables are independent of x (zonally symmetric), the geostrophic flow should be purely zonal, therefore, at the APBL top the geostrophic wind would be

$$u_{G*} = u_{G*}(y), \quad v_{G*} = 0 \tag{38}$$

The scale of thermally forced surface winds (Chu, 1989) is

$$U_T \equiv \frac{g\delta\Delta T}{2\Omega L_y \theta_0} \tag{39}$$

where $\delta = (\nu/\Omega)^{1/2}$, is the Ekman depth, ν is the atmospheric vertical eddy viscosity, Ω is the angular velocity of the earth's rotation, and $\Delta T/L_y$ is the characteristic SSAT gradient. If $\delta \cong 1$ km (Holton, 1972), $\Delta T = 14°$k, $L_y \cong 2000$ km (Robinson et al, 1977), and $\theta_0 \cong 288°$k, the scale for the thermally driven surface wind (U_T) approaches 3 m/s, and the scale of the geostrophic wind at the APBL top (U) can reasonably be assumed to be 10 m/s. Therefore, if we completely neglect this thermally driven surface wind in ocean models, we will make almost 30% error in the surface wind forcing.

Based on the K-closure APBL model proposed by Kuo (1973), Chu (1992) found these wind and temperature fields are:

$$u(y,z) = \sum_n \left[-b_n \exp(-\sqrt{2\gamma}\, z) + 2f_0 \sum_{j=1}^{3} \frac{a_{nj}\lambda_{nj}}{\lambda_{nj}^2 - 2\lambda} \exp(\lambda_{nj} z) \right] \sin k_n \pi y \tag{40}$$

$$\theta(y,z) = \sum_n \left[\frac{\sqrt{2\gamma}\, f_0 b_n}{k_n \pi} \exp(-\sqrt{2\gamma}\, z) + 2k_n \pi \tilde{R}i \sum_{j=1}^{3} \frac{a_{nj}}{\lambda_{nj}^2 - 2\gamma} \exp(\lambda_{nj} z) \right] \cos k_n \pi y \tag{41}$$

$$v(y,z) = -\frac{\partial \psi}{\partial z} = -\sum_n \sum_{j=1}^{3} a_{nj}\lambda_{nj} \exp(\lambda_{nj} z) \sin k_n \pi y \tag{42}$$

evaluated at z=0, i.e.,

$$u_{sn} = -b_n + 2f_0 \sum_{j=1}^{3} \frac{a_{nj}\lambda_{nj}}{\lambda_{nj}^2 - 2\gamma} + \mu u_{Gn}, \quad n = 1, 2, \ldots \tag{43}$$

$$v_{sn} = -\sum_{j=1}^{3} a_{nj}\lambda_{nj} \tag{44}$$

$$\theta_{sn} = \frac{\sqrt{2\gamma}\, f_0 b_n}{k_n \pi} + 2k_n \pi \tilde{R}i \sum_{j=1}^{3} \frac{a_{nj}}{\lambda_{nj}^2 - 2\gamma} \tag{45}$$

where γ is the nondimensional decay rate ($\gamma = 0.01$, denoting 100 day decay time scale) for Rayleigh friction and Newtonian cooling, $f_0 = \sin\phi$, is the nondimensional Coriolis parameter, taken as locally constant except very close to the equator, ϕ is latitude, and

$$\tilde{Ri} = Ri(\delta/H_a)^2 \tag{46}$$

is the generalized Richardson number. $H_a \cong 10$ km, is the thickness, and

$$Ri \equiv \left(\frac{H_a N}{2L_y\Omega}\right)^2 \tag{47}$$

is the Richardson number. Here, N is the Brunt-Vaisala frequency. $\lambda_{nj}(j = 1, 2, 3)$ are the eigenvalues. a_{n1}, a_{n2}, and a_{n3} are integral constants. ψ is the streamfunction.

The boundary condition in the vertical are listed as follow. The dependent variables should remain finite as z $\rightarrow \infty$, i.e.,

$$\lim_{n\to\infty}\left(|\psi|, \left|\frac{\partial\psi}{\partial z}\right|, |u|, |\theta|\right) < \infty \tag{48}$$

The surface boundary conditions (at z = 0) are

$$\psi|_{z=0}=0, \quad \mu u_G + u = M\frac{\partial u}{\partial z}, \quad v = M\frac{\partial v}{\partial z}, \quad \theta - M_1\frac{\partial\theta}{\partial z} = \theta_s \tag{49}$$

where M, M_1 are given constants, and

$$\mu \equiv U/U_T \cong 3.33 \tag{50}$$

the parameter $M = 0.5$, which is a measure of the effective depth of the constant stress sub-layer (Kuo, 1973).

The surface boundary condition (48) and (49) leads to (assuming $M_1 = 0$)

$$\sum_{j=1}^{3} a_{nj} = 0 \tag{51}$$

$$u_{sn} = \sqrt{2\gamma}\, Mb_n + 2f_0 M \sum_{j=1}^{3} \frac{a_{nj}\lambda_{nj}^2}{\lambda_{nj}^2 - 2\gamma} \tag{52}$$

$$\sum_{j=1}^{3} \lambda_{nj}(1 - M\lambda_{nj})\, a_{nj} = 0, \quad or \quad \sum_{j=1}^{3} \lambda_{nj}^2 a_{nj} = -\frac{v_{sn}}{M} \tag{53}$$

Solving the linear algebraic equation (44), (51), and (53) with respect to a_{n1}, a_{n2}, and a_{n3}, we obtain

$$a_{n1} = -\frac{l_{n1}}{l_n} v_{sn}, \quad a_{n2} = -\frac{l_{n2}}{l_n} v_{sn}, \quad a_{n3} = -\frac{l_{n3}}{l_n} v_{sn} \tag{54}$$

where

$$l_{n1} \equiv \begin{vmatrix} 0 & 1 & 1 \\ 1 & \lambda_{n2} & \lambda_{n3} \\ 1/M & \lambda_{n2}^2 & \lambda_{n3}^2 \end{vmatrix} \tag{55}$$

$$l_{n2} \equiv \begin{vmatrix} 1 & 0 & 1 \\ \lambda_{n1} & 1 & \lambda_{n3} \\ \lambda_{n2}^2 & 1/M & \lambda_{n3}^2 \end{vmatrix} \tag{56}$$

$$l_{n3} \equiv \begin{vmatrix} 1 & 1 & 0 \\ \lambda_{n1} & \lambda_{n2} & 1 \\ \lambda_{n1}^2 & \lambda_{n2}^2 & 1/M \end{vmatrix} \tag{57}$$

$$l_n \equiv \begin{vmatrix} 1 & 1 & 1 \\ \lambda_{n1} & \lambda_{n2} & \lambda_{n3} \\ \lambda_{n1}^2 & \lambda_{n2}^2 & \lambda_{n3}^2 \end{vmatrix} \tag{58}$$

Elimination of b_n from (43), (45), and (52) leads to

$$u_{sn} = -R_{1n}\theta_{sn} + H_{1n}u_{Gn} \tag{59}$$

$$v_{sn} = -R_{2n}\theta_{sn} + H_{2n}u_{Gn} \tag{60}$$

where

$$R_{2n} = \frac{k_n\pi}{\sqrt{2\gamma}\ f_0}(1 + \sqrt{2\gamma}\ M)\frac{1}{J_n} \tag{61}$$

$$R_{1n} = I_nR_{2n} - \frac{k_n\pi M}{f_0} \tag{62}$$

$$H_{1n} = \mu\frac{I_n}{J_n}, \qquad H_{2n} = \frac{\mu}{J_n} \tag{63}$$

where

$$I_n \equiv \left(\frac{2Mk_n^2\pi^2\tilde{R}i}{f_0} - 4Mf_0\gamma\right)\sum_{j=1}^{3}\frac{l_{nj}}{l_n(\lambda_{nj}^2 - 2\gamma)} \tag{64}$$

$$J_n \equiv \left[\frac{2k_n^2\pi^2\tilde{R}i}{f_0\sqrt{2\gamma}}(1 + \sqrt{2\gamma}\ M) - 4f_0M\gamma\right]\sum_{j=1}^{3}\frac{l_{nj}}{l_n(\lambda_{nj}^2 - 2\gamma)} + 2f_0\sum\frac{l_{nj}\lambda_{nj}}{l_n(\lambda_{nj}^2 - 2\gamma)} \tag{65}$$

The solutions (59), and (60) show that the surface winds (u_{sn}, v_{sn}) are driven mechanically by the geostrophic winds, u_{Gn}, and thermally by the surface thermal conditions, $-R_{1n}\theta_{sn}$, and $-R_{2n}\theta_{sn}$.

The coefficient in (59) and (60) R_{1n}, R_{2n}, H_{1n}, and H_{2n} for different k_n can be computed by using the dependence of eigenvalues λ_{n1}, λ_{n2}, and λ_{n3} on k_n for

$$\tilde{R}i = 0.01 \tag{66}$$

Non-zero values for these coefficients indicate that only two can be prescribed among the four variables u_{sn}, v_{sn}, θ_{sn}, and u_{Gn}, the other two should be derived from (59) and (60). Thus, (59) and (60) can be treated as a compatibility condition among these four variables. Obviously, it is over-specified if we prescribe both surface wind stress and buoyancy forcing in ocean numerical models.

We can use (59) and (60) to verify the consistency between buoyancy forcing (3) and surface wind (4) which is used in the Davey (1983) model. Here, $T_A(y) \neq 0$, the Fourier cosine series of T_A is

$$T_A(y) = (T_N - T_S) \sum_n \theta_{sn} \cos n\pi y \tag{67}$$

The surface winds (u_s, v_s) are set to zero, therefore, the components of their Fourier sine series should also be zero, i.e.,

$$u_{sn} = 0, \qquad v_{sn} = 0 \tag{68}$$

Non-zero values of

$$\varphi_n \equiv \frac{(H_{1n}R_{2n} - H_{2n}R_{1n})}{H_{2n}} \tag{69}$$

shows that the linear algebraic equations (59) and (60) about θ_{sn} and u_{Gn} only have zero solutions, i.e., $\theta_{sn} = 0$, $u_{Gn} = 0$, when $u_{sn} = 0$, $v_{sn} = 0$. Therefore, the thermal forcing (3) is not compatible with the surface wind forcing (4).

Purely zonal surface winds are commonly used in ocean models, such as the surface boundary conditions (5). Here, three variables u_s, v_s, and T_A are prescribed. We expand these surface variables into Fourier sine and cosine series

$$(u_s,\ v_s) = \sqrt{\frac{\tau_0}{\rho_a C_D}} \sum_n (u_{sn},\ v_{sn}) \sin n\pi y, \quad v_{sn} = 0 \tag{70}$$

$$T_A = (\Delta T) \sum_n \theta_{sn} \cos n\pi y \tag{71}$$

$$u_G = U \sum_n u_{Gn} \sin n\pi y \tag{72}$$

The Fourier components u_{sn}, v_{sn}, θ_{sn}, and u_{Gn} should satisfy the two linear algebraic equations (59) and (60):

$$u_{sn} = -R_{1n}\theta_{sn} + H_{1n}u_{Gn} \tag{73}$$

$$0 = -R_{2n}\theta_{sn} + H_{2n}u_{Gn} \tag{74}$$

which shows that purely zonal surface winds appear only when the surface thermal forcing is balanced by the geostrophic forcing

$$\theta_{sn} = \frac{H_{sn}}{R_{sn}} u_{Gn} \tag{75}$$

Elimination of u_{Gn} from these two equations leads to a relationship between u_{sn} and θ_{sn}, (Chu, 1992):

$$u_{sn} = -\varphi_n \theta_{sn} \tag{76}$$

which is the compatibility condition for zonally symmetric zonal wind and SSAT fields. Independently prescribing surface wind and SSAT fields, such as in (5), violates this condition and therefore, is inconsistent.

IV. ERRORS IN NUMERICAL INTEGRATION OF THE MOM MODEL CAUSED BY INCOMPATIBLE FORCING

A. SURFACE BOUNDARY CONDITIONS

The MOM model and its parameters have been discussed in Chapter II. Two kinds (compatible and incompatible) of surface boundary conditions (SST, salinity, wind stress in x direction, and wind stress in y direction) were used in MOM model to find the differences between the results of the two conditions.

The incompatible surface boundary condition (SST, salinity, wind stress in x direction, and wind stress in y direction) which is used in the general circulation model by Marotzke and Willebrand (1991) is shown in figure 1a. The zonal (eastward) wind stress (solid curve) and the apparent atmospheric temperature in degrees celsius (dashed curve) are functions of latitude and symmetric about the equator, so they are only shown for one hemisphere.

The sea surface temperature (SST) in °C is symmetric about the equator, and follows a cosine law in latitude with a difference of 27°C between high and low latitudes (Fig. 1b). The salinity is analogous to the sea surface temperature and symmetric about the equator. The salinity also follows a cosine law in latitude with amplitude 2.5 psu (Fig.1c).

Many independently and simple prescribed wind and buoyancy forcing in ocean models have a similar form as used by Marotzke and Willebrand (1991) in a steady-state wind and thermally forced ocean circulation model (Fig. 1, 2 and 3).

The latitudinal surface atmospheric temperature gradient generates extra surface winds (u_T, v_T). The scale of this thermally driven surface winds is given by (39). Corresponding to SSAT field described in figure 1b, the thermally driven surface winds can be predicted by a K-closure Atmospheric Planetary Boundary Layer (APBL) model (Chu, 1989). From wind and temperature fields (40), (41) and (42), we obtain

$$\begin{bmatrix} u_T \\ v_T \end{bmatrix} = \frac{U_T}{G_T} \begin{bmatrix} \cos\alpha & -\sin\alpha \\ \sin\alpha & \cos\alpha \end{bmatrix} \nabla\theta_a|_{z=0} \qquad (77)$$

where α is the deflection angle (angle between V_T and $\nabla\theta_a \mid_{z=0}$). The wind field with the thermally driven component (i.e., $u+u_T$, v_T) is illustrated by solid curves and without the thermally driven component is illustrated by dashed curves in figure 2 and 3.

From figure 2 and 3, we compute the Ekman current change due to compatible forcing (Fig. 4). The result in a stronger westward and poleward current between about 5° and 30° latitude in both hemisphere. We also compute the wind stress curl for the wind field with and without thermally driven component.

Wind stress curl for forcing without thermally driven component:

$$\vec{K} \cdot Curl\ \vec{\tau} = \frac{\partial \tau_y}{\partial x} - \frac{\partial \tau_x}{\partial y} \qquad (78)$$

τ_y is independent of x, so

$$\vec{K} \cdot Curl\ \vec{\tau} = -\frac{\partial \tau_x}{\partial y} \tag{79}$$

Wind stress curl for forcing with thermally driven component:

$$\vec{K} \cdot Curl\ \vec{\tilde{\tau}} = \frac{\partial \tilde{\tau}_y}{\partial x} - \frac{\partial \tilde{\tau}_x}{\partial y} \tag{80}$$

$\vec{\tilde{\tau}}_y$ is independent with x, so

$$\vec{K} \cdot Curl\ \vec{\tilde{\tau}} = -\frac{\partial \tilde{\tau}_x}{\partial y} \tag{81}$$

The difference between the wind stress curl for wind field with and without thermally driven component is not negligible.

B. ERRORS CAUSED BY INCOMPATIBLE WIND AND BUOYANCY FORCING

We consider a rectangular ocean of uniform depth in the MOM model. The thickness (m) and depth (m) in the vertical of the 15 level MOM model is specified as below:

Level	Thickness (m)	Depth (m)
1	30.00	30.00
2	46.15	76.15
3	68.93	145.08
4	99.93	254.01

5	140.63	385.64
6	192.11	577.75
7	254.76	832.51
8	327.95	1160.46
9	409.81	1570.27
10	497.11	2067.38
11	585.36	2652.74
12	669.09	3321.83
13	742.41	4064.24
14	799.65	4863.89
15	836.10	5699.99

1. The total northward transport of heat

The total northward transport of heat, which was calculated by compatible surface wind stress and buoyancy forcing, after 3, 6, 9, and 12 years is shown in figure 5. The difference in the total northward transport of heat between compatible and incompatible surface wind stress and buoyancy forcing after 3, 6, 9, and 12 years is provided in figure 6. In all plots the difference is computed from the compatible forcing run minus the incompatible forcing run.

The total northward transport of heat, which was calculated by compatible surface wind stress and buoyancy forcing, after 51, 54, 57, and 60 years is shown in figure 7. The difference in the total northward transport of heat between compatible and incompatible surface wind stress and buoyancy forcing after 51, 54, 57, and 60 years is provided in figure 8.

When the northward transport of heat by compatibility consideration is large in figure 5, the difference in the northward transport of heat, shown in figure 6, due to the incompatibility forcing, is also large. The error reaches to 21% after 51 year's integration. The difference in the northward transport of heat between the compatibility and incompatibility consideration increases with the integration time.

In northern (southern) hemisphere, an additional northeasterly (southeastly) wind stress exists in the compatible forcing case (Fig. 2, 3). Therefore, an extra northwest (southwest) Ekman transport should appear when we use the compatible forcing (Fig. 4).

2. The total northward transport of salt

The total northward transport of salt which was calculated by compatible surface wind stress and buoyancy forcing, after 3, 6, 9, and 12 years is shown in figure 9. The difference in the total northward transport of salt between compatible and incompatible surface wind stress and buoyancy forcing after 3, 6, 9, and 12 years is provided in figure 10.

The total northward transport of salt which was calculated by compatible surface wind stress and buoyancy forcing, after 51, 54, 57, and 60 years is shown in figure 11. The difference in the total northward transport of salt between compatible and incompatible surface wind stress and buoyancy forcing after 51, 54, 57, and 60 years is provided in figure 12.

When northward transport of salt by compatibility consideration is large in figure 9, the difference in the northward transport of salt in figure 10, due to the

incompatibility forcing, is also large. The error reaches to 16% after 51 year's integration. The difference in the northward transport of salt between the compatibility and incompatibility consideration increases with the integration time.

3. The meridional mass transport

The meridional mass transport, which was calculated by compatible surface wind stress and buoyancy forcing, after 30 years is shown in figure 13. The difference in the meridional mass transport between compatible and incompatible surface wind stress and buoyancy forcing after 30 years is provided in figure 14.

The meridional mass transport, which was calculated by compatible surface wind stress and buoyancy forcing, after 60 years is shown in figure 15. The difference in the meridional mass transport between compatible and incompatible surface wind stress and buoyancy forcing after 60 years is provided in figure 16.

From above, the latitudinal distribution of meridional mass transport after 60 years integration indicates that the compatibility consideration meridional mass transport is larger than that of incompatibility consideration in all latitudes of the northern hemisphere and smaller in all latitudes of southern hemisphere. The difference between the two consideration (compatibility and incompatibility) increases with the latitude.

In figure 16, the difference of mass transport is strong between 25°S and 25°N due to the extra Ekman transport when the compatible forcing is used (Fig. 4). The error is more then 5 Sverdrup in northward mass transport. In deeper sea water it is about 5 Sverdrup less.

4. Meridional section profile of θ

The meridional section profile of θ at 160°E after 60 years is shown in figure 17 and the difference is provided in figure 18. The meridional section profile of θ at 160°W after 60 years is shown in figure 19 and the difference is provided in figure 20. The meridional section profile of θ at 120°W after 60 years is shown in figure 21 and the difference is provided in figure 22.

From the difference of meridional section profile of θ in figure 18, 20, and 22, we can see that the potential temperature θ is always lower in the compatible forcing than in incompatible forcing near the equator. The errors caused by incompatible forcing in upper is larger than that in the deeper sea water.

The mass transport is northward in north hemisphere and southward in south hemisphere. Thus divergence occurs near the equator. So the cold deeper sea water moves upward toward the surface to make the temperature lower near the equator.

5. Meridional section profile of v velocity

The meridional section profile of v velocity at 160°E after 60 years is shown in figure 25, and the difference is provided in figure 26. The meridional section profile of v velocity at 160°W after 60 years is shown in figure 27, and the difference is provided in figure 28. The meridional section profile of v velocity at 120°W after 60 years is shown in figure 29, and the difference is provided in figure 30.

From the meridional section profiles of v velocity in figure 25, 27, and 29, the v velocity is positive from the equator to about 25°N where the velocity changes

direction (opposite sign) toward high latitude. The v velocity in the southern-hemisphere is compared with the relation in the northern-hemisphere.

From figure 14 and 16, the latitudinal distribution of meridional mass transport after 60 years integration indicates that the compatibility consideration meridional mass transport is larger than that of incompatibility consideration in all latitudes of the northern hemisphere and smaller in all latitudes of southern hemisphere. This is consistent with figure 4, which shows an extra northwest (southwest) Ekman transport in northern (southern) hemisphere when the compatible forcing is used.

Therefore, we see the difference of meridional section profile of v velocity in figure 24, 26, and 28, the v velocity, which is due to compatible forcing correction, is always stronger in the northern-hemisphere than that due to incompatible forcing influence. In the southern-hemisphere the resulting v velocity which is integrated by compatible forcing is found to be weak. The errors by incompatible forcing is most obvious in the upper sea water. The errors is nearly 25%.

6. Meridional section profile of w velocity

The meridional section profile of w velocity at 160°E after 60 years is shown in figure 29, and the difference is provided in figure 30. The meridional section profile of w velocity at 160°W after 60 years is shown in figure 31, and the difference is provided in figure 32. The meridional section profile of w velocity at 120°W after 60 years is shown in figure 33, and the difference is provided in figure 34.

From the meridional section profiles of w velocity in figure 29, 31, and 33, the w velocity has large variation in longitude (i.e., section to section) indicating the

effect of transients (eddies). The w velocity profile of deep water is more complex than that of upper sea water. From the difference of meridional section profile of w velocity in figure 30, 32, and 34, the w velocity, which is due to incompatible forcing influences, has more errors near the equator than that of high latitude. The errors is about 16%.

7. Difference at some random points

a. θ at 160°E, 0°N on level 2

The difference in θ for depth of 76.15 meters (level 2) at 160°E, 0°N is shown in figure 35. The error for θ in the first three years is about 6% due to incompatible forcing influences. This error increases to 7% after about 10 years integration.

An extra northwest (southwest) Ekman transport appears in the northern (southern) hemisphere when the compatible forcing is used. Thus an additional horizontal divergence occurs near the equator. Causing an extra amount of cold deeper sea water moves upward toward the surface making the temperature lower near the equator in the compatible case. Therefore, at depth of 76.15 meters (level 2) at 160°E, 0°N the θ by the compatible forcing in the whole integration time of 60 years is always lower than that due to incompatible forcing influences.

b. V velocity at 160°E, 5°S on level 2

The difference in v velocity for depth of 76.15 meters (level 2) at 160°E, 5°S is provided in figure 36. The error in v velocity in the first three years is about

26% due to incompatible forcing influences. This error increases to about 28% after about 8 years integration.

From the meridional section profiles of v velocity in figure 23, 25, and 27, the v velocity is positive from the equator to about 25°N where the velocity changes direction (opposite sign) toward high latitude. The v velocity in the southern-hemisphere is compared with the relation in the northern-hemisphere.

From figure 14 and 16, the latitudinal distribution of meridional mass transport after 60 years integration indicates that the compatibility consideration meridional mass transport is larger than that of incompatibility consideration in all latitudes of the northern hemisphere and smaller in all latitudes of southern hemisphere. This is consistent with figure 4, which shows an extra northwest (southwest) Ekman transport in northern (southern) hemisphere when the compatible forcing is used.

Therefore, at depth of 76.15 meters (level 2) at 160°E, 5°S the v velocity by the compatible forcing in the whole integration time of 60 years is always weaker than that due to incompatible forcing influences.

c. V velocity at 160°E, 10°S on level 2

The difference in v velocity for depth of 76.15 meters (level 2 at 160°E, 10°S can be seen in figure 37. The error in v velocity in the first three years is about 23% which is due to incompatible forcing influences. This increases the error to 28% after about 8 years integration. At depth of 76.15 meters (level 2) at 160°E, 10°S the v velocity by the compatible forcing in the whole integration time of 60 years is always weaker than that due to incompatible forcing influences.

d. W velocity at 160°E, 10°N on level 5

The difference in w velocity for depth of 385.64 meters (level 5) at 160°E, 10°N is illustrated in figure 38. The error of w velocity in the first three years is about 16% due to incompatible forcing influences. This error decreases to 10% after about 8 years integration. At depth of 385.64 meters (level 5) at 160°E, 10°N the w velocity by the compatible forcing is always stronger than that due to incompatible forcing influences after 6 years integration.

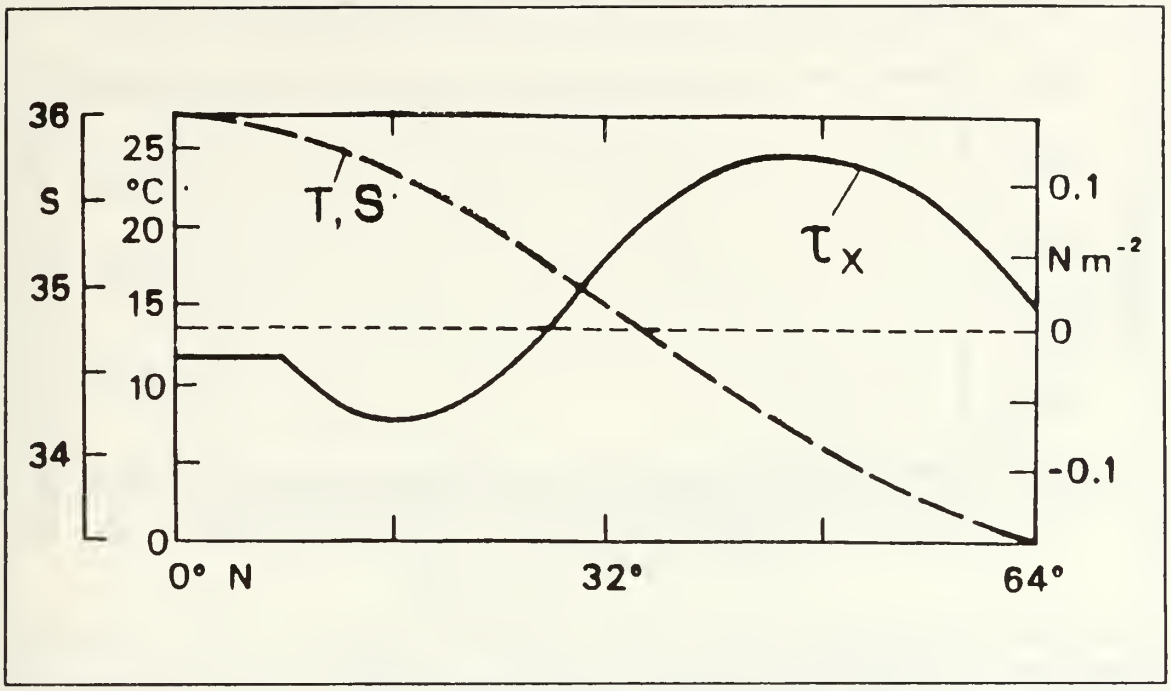

Figure 1a. The surface forcing fields which were used by Marotzke and Willebrand (1991).

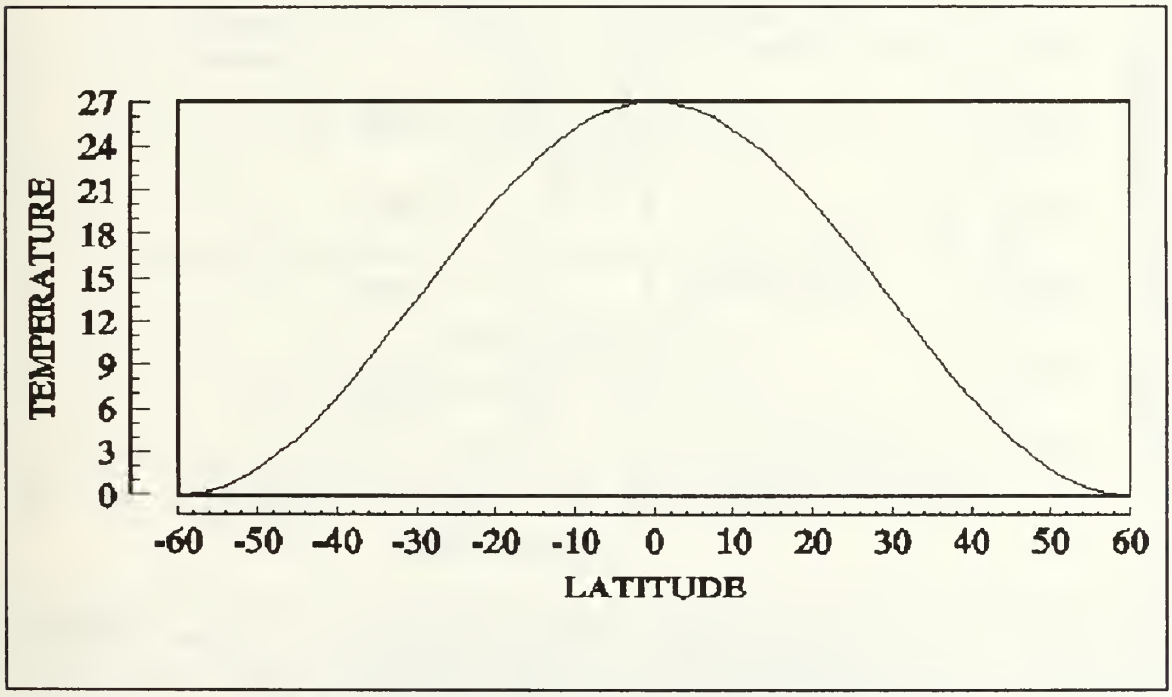

Figure 1b. Zonal mean values of observed sea surface temperature (°C), used by Marotzke and Willebrand (1991).

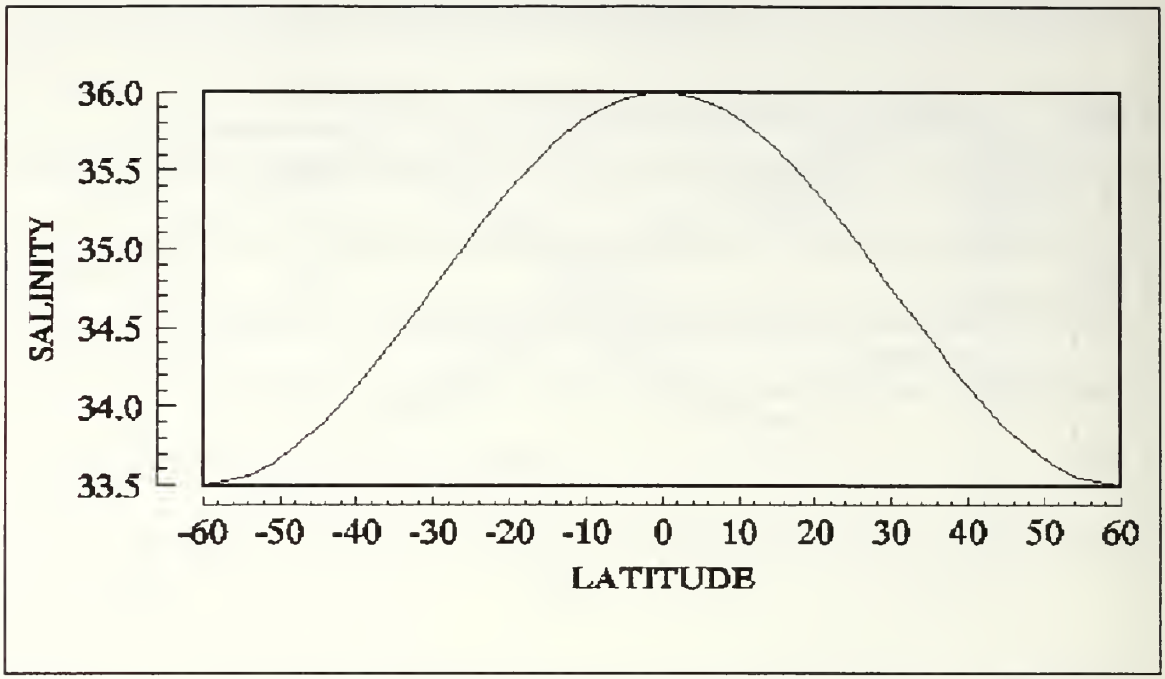

Figure 1c. Zonal mean values of observed salinity (psu), used by Marotzke and Willebrand (1991).

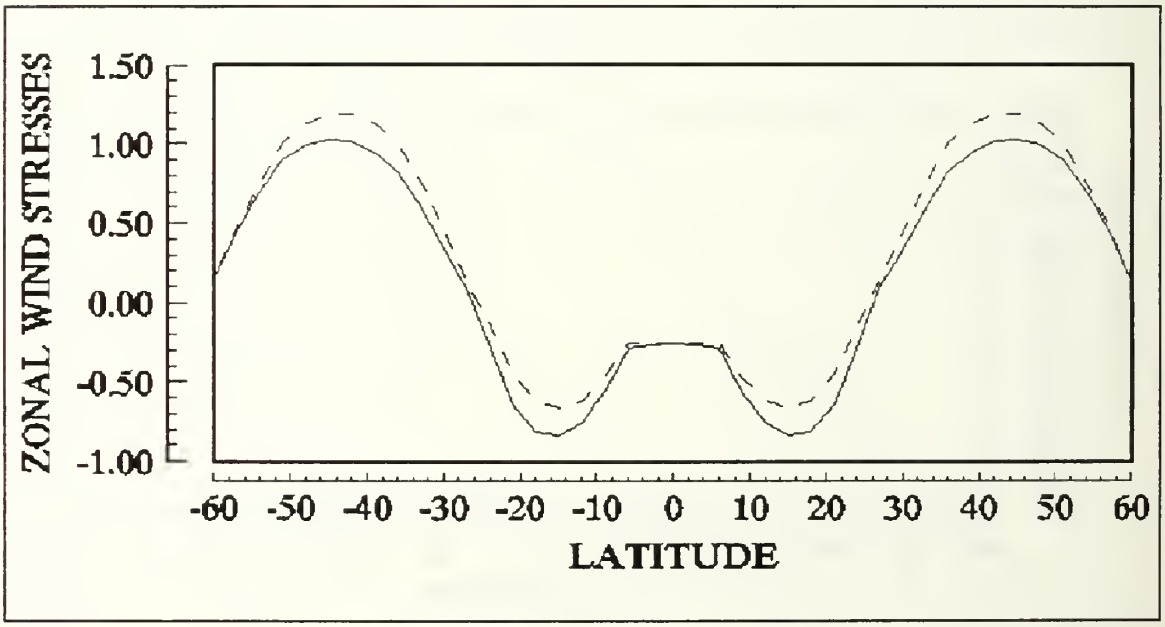

Figure 2. Surface zonal wind stresses (dynes/cm^2) as functions of latitude. (a) without thermally driven surface winds (dash curve). (b) with thermally driven surface winds (solid curve).

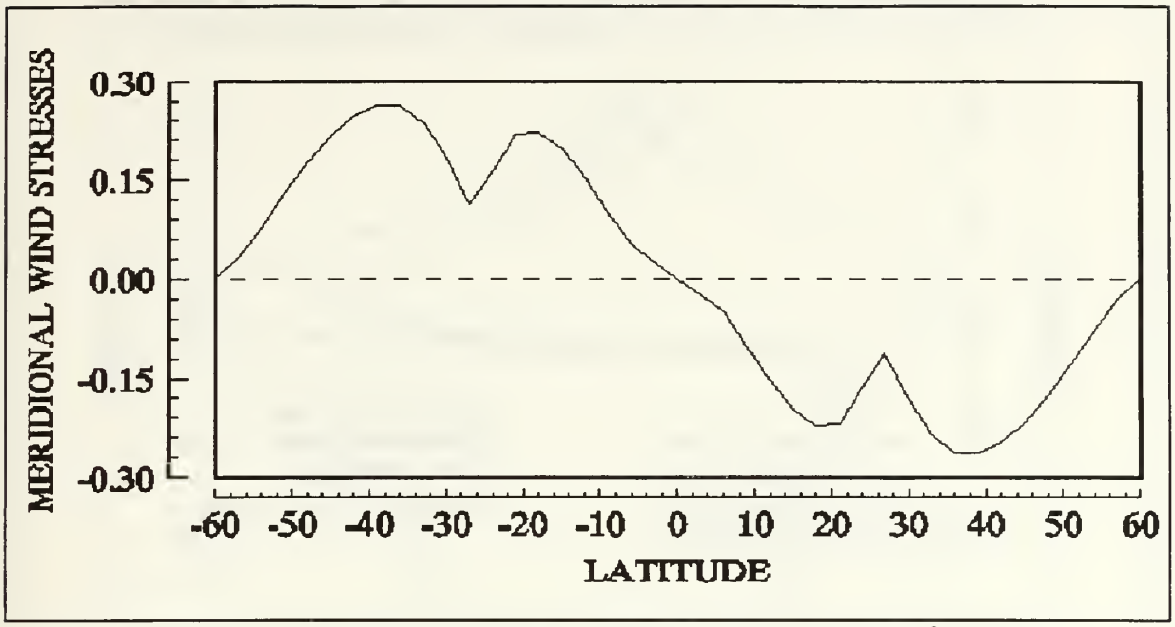

Figure 3. Surface meridional wind stresses (dynes/cm^2) as functions of latitude. (a) without thermally driven surface winds (dashed curve). (b) with thermally driven surface winds (dashed curve).

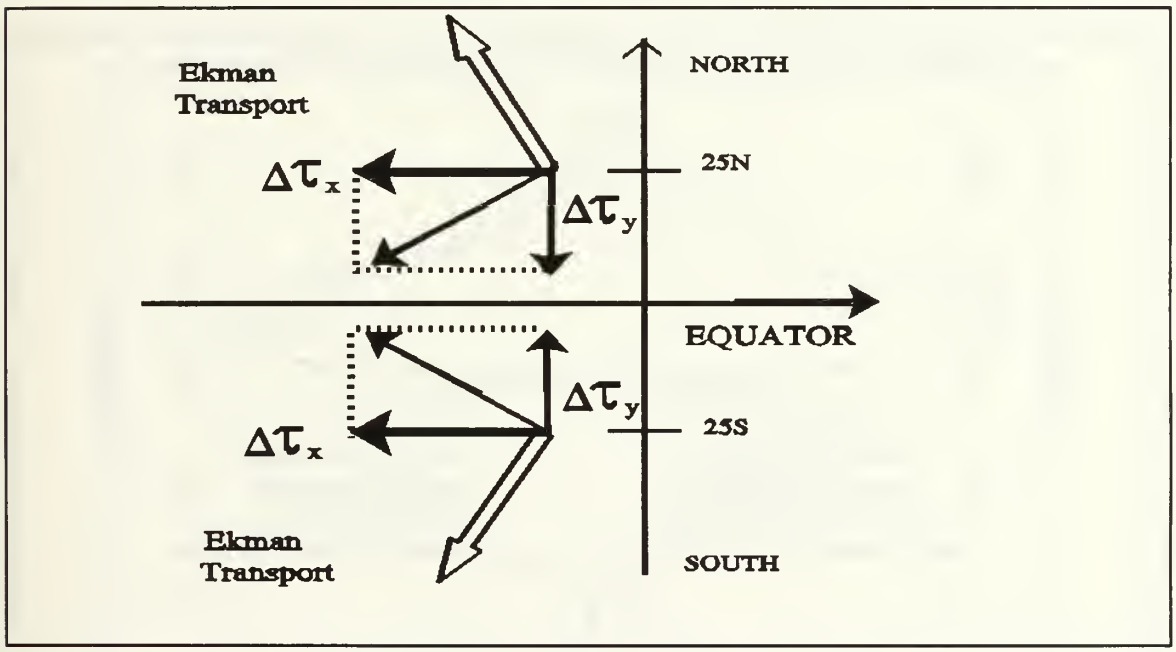

Figure 4. The Ekman current change near 25°N and 25°S due to compatible forcing. The solid arrows show the change in the wind stress (Figs. 2 and 3) and the double arrows show the resulting change in the surface Ekman current.

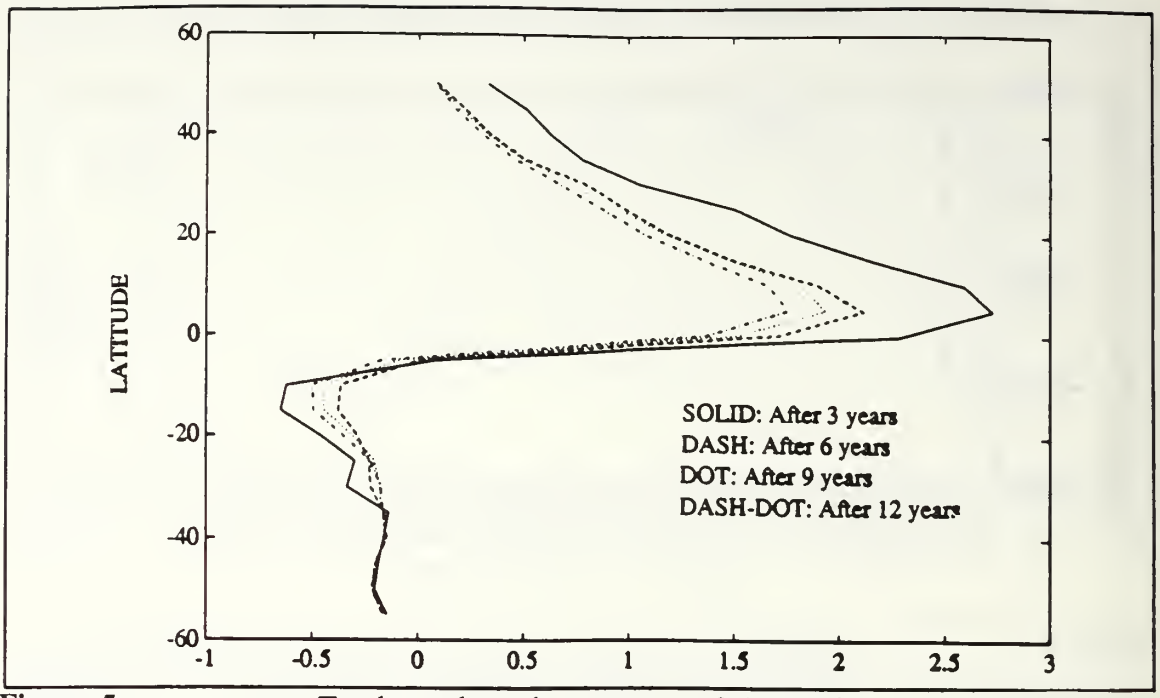

Figure 5. Total northward transport of heat after 3, 6, 9, 12 years integration. ($\times 10^{15}$ Watts).

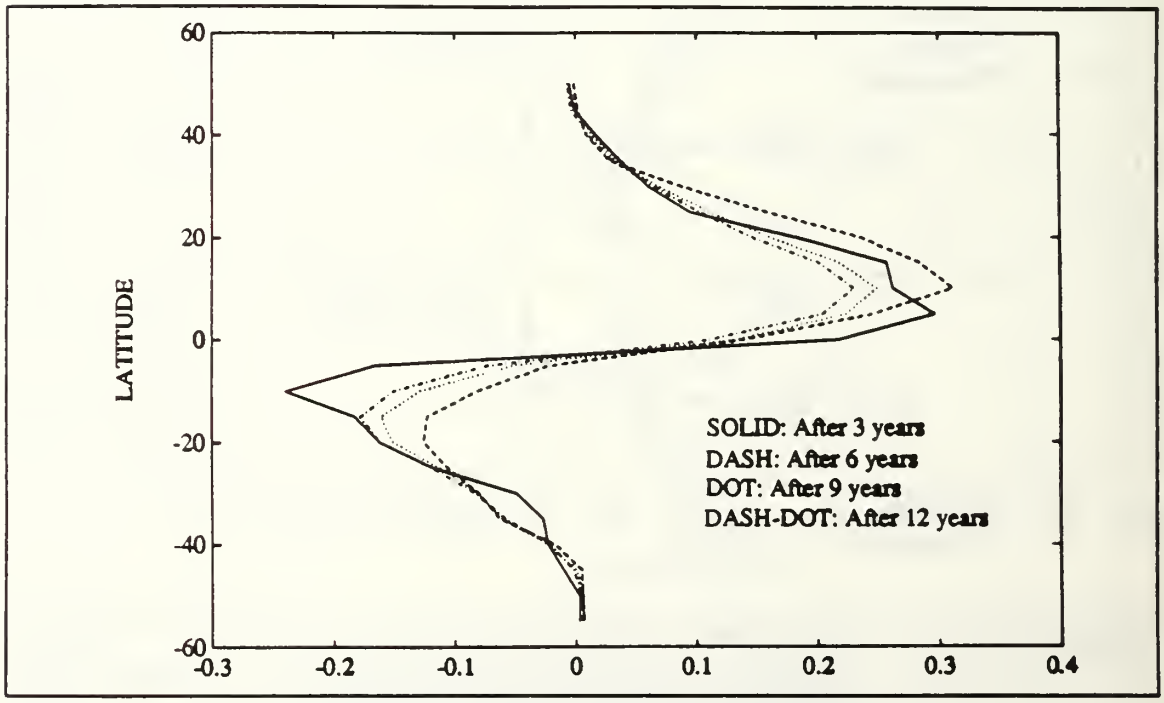

Figure 6. Difference of total northward transport of heat after 3, 6, 9, 12 years integration. ($\times 10^{15}$ Watts).

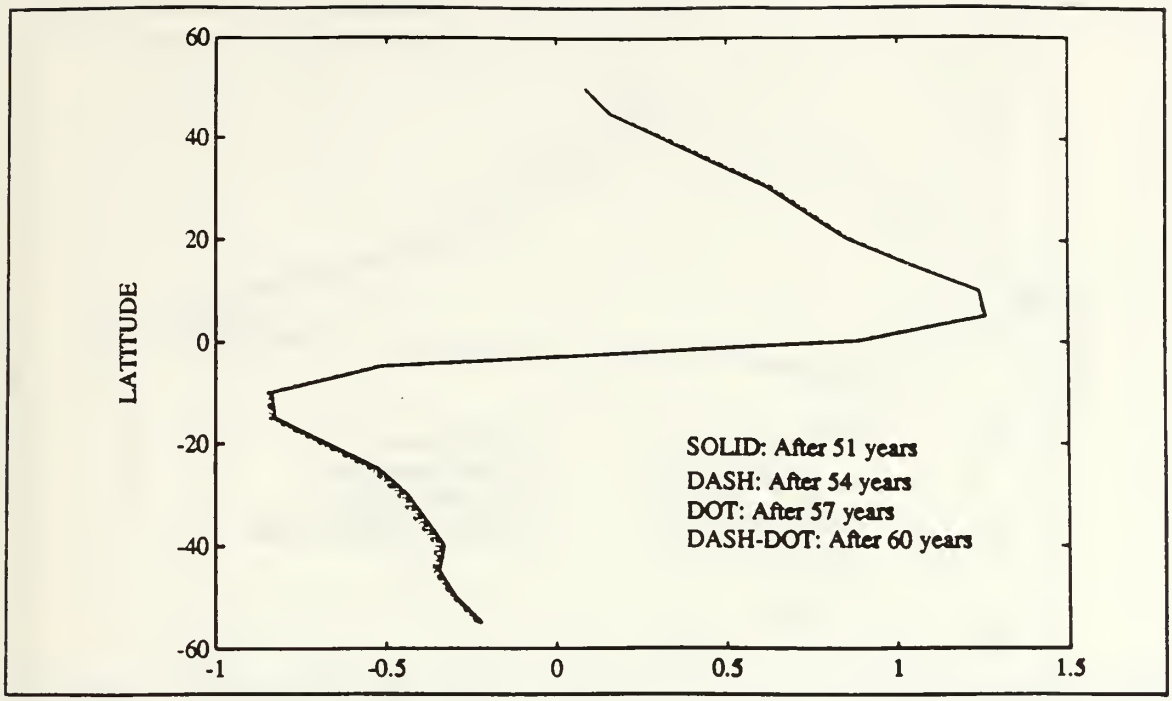

Figure 7. Total northward transport of heat after 51, 54, 57, 60 years integration. ($\times 10^{15}$ Watts).

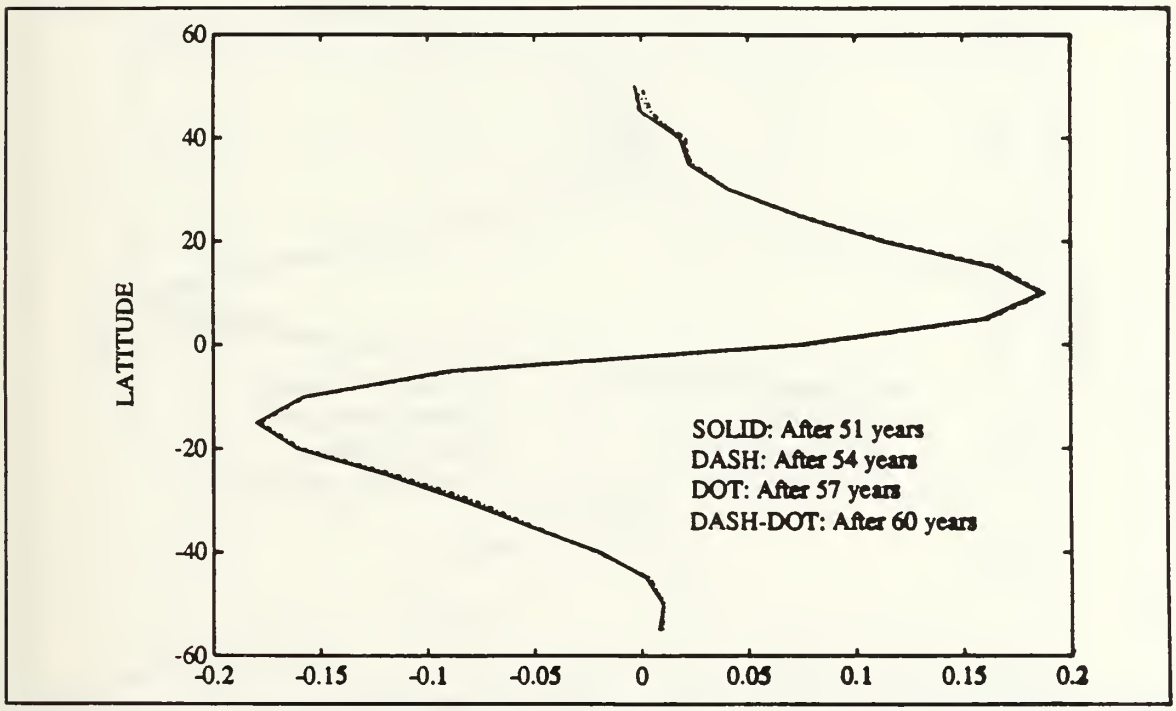

Figure 8. Difference of total northward transport of heat after 51, 54, 57, 60 years integration ($\times 10^{15}$ Watts).

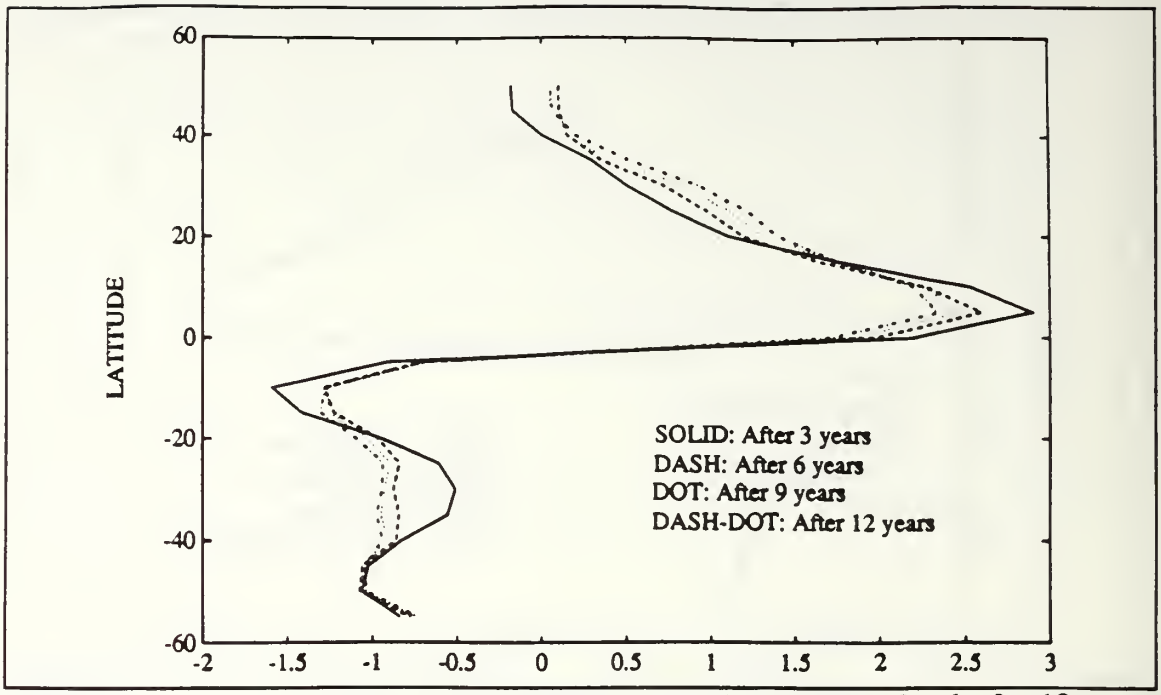

Figure 9. Total northward transport of salt after 3, 6, 9, 12 years integration. ($\times 10^{10}$ cm^3/sec).

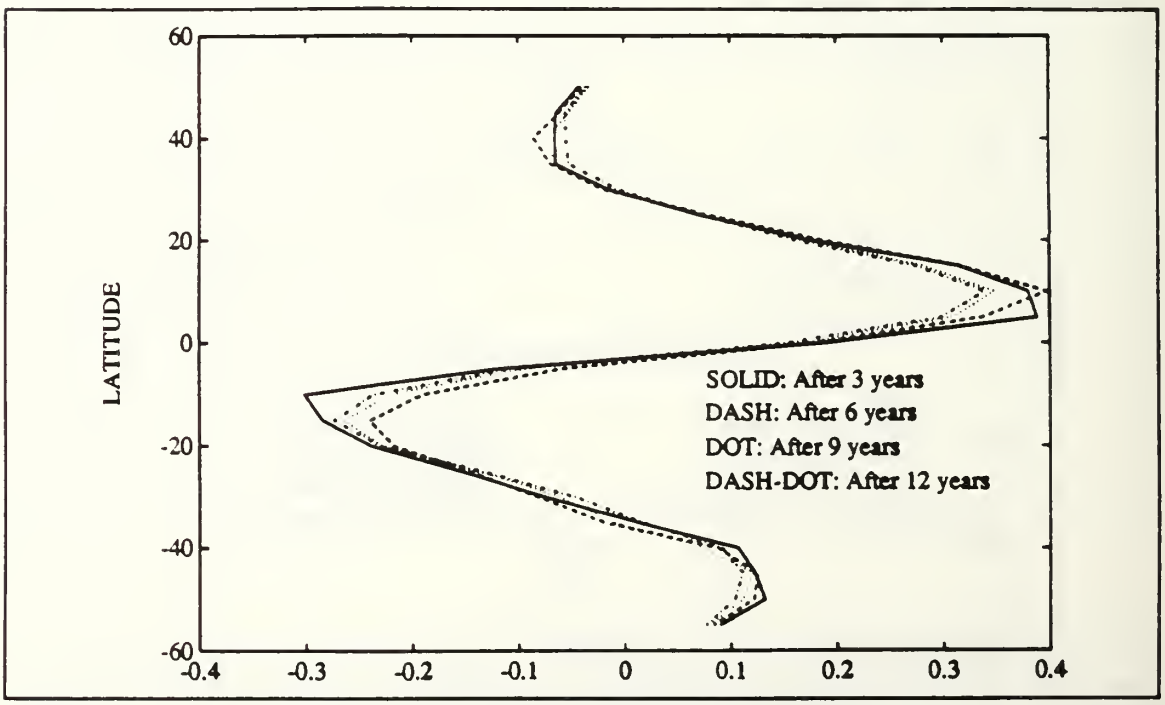

Figure 10. Difference of total northward transport of salt after 3, 6, 9, 12 years integration. ($\times 10^{10}$ cm^3/sec).

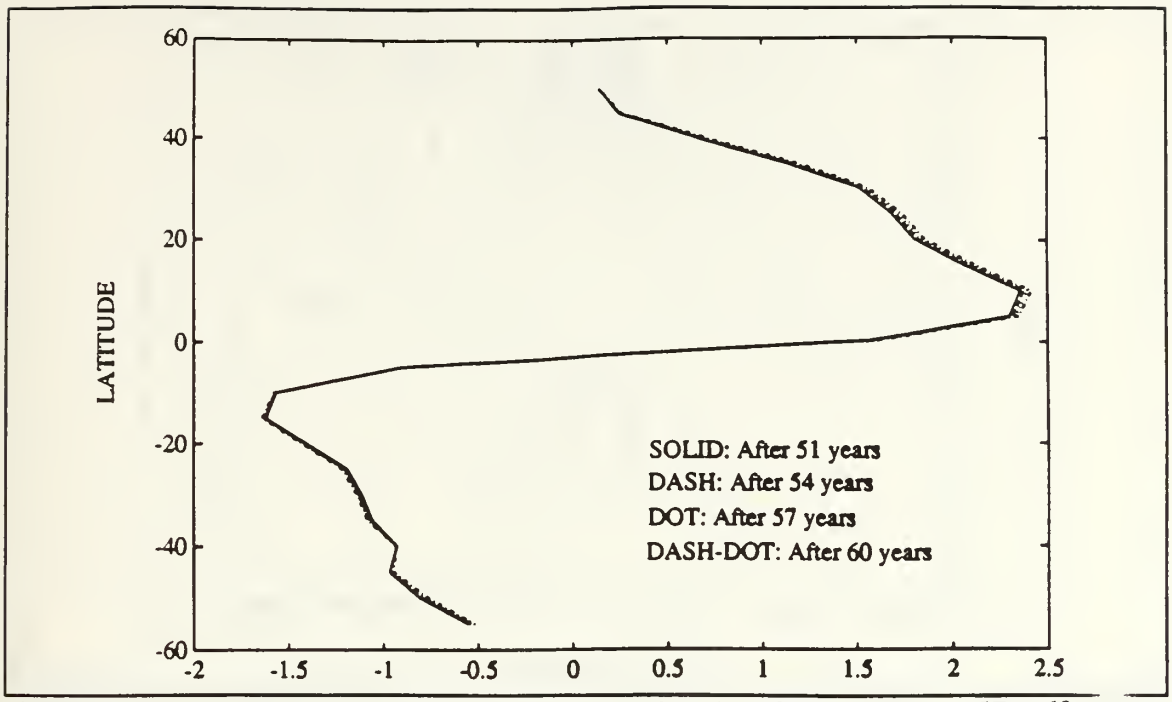

Figure 11. Total northward transport of salt after 51, 54, 57, 60 ars integration. ($\times 10^{10}$ cm^3/sec).

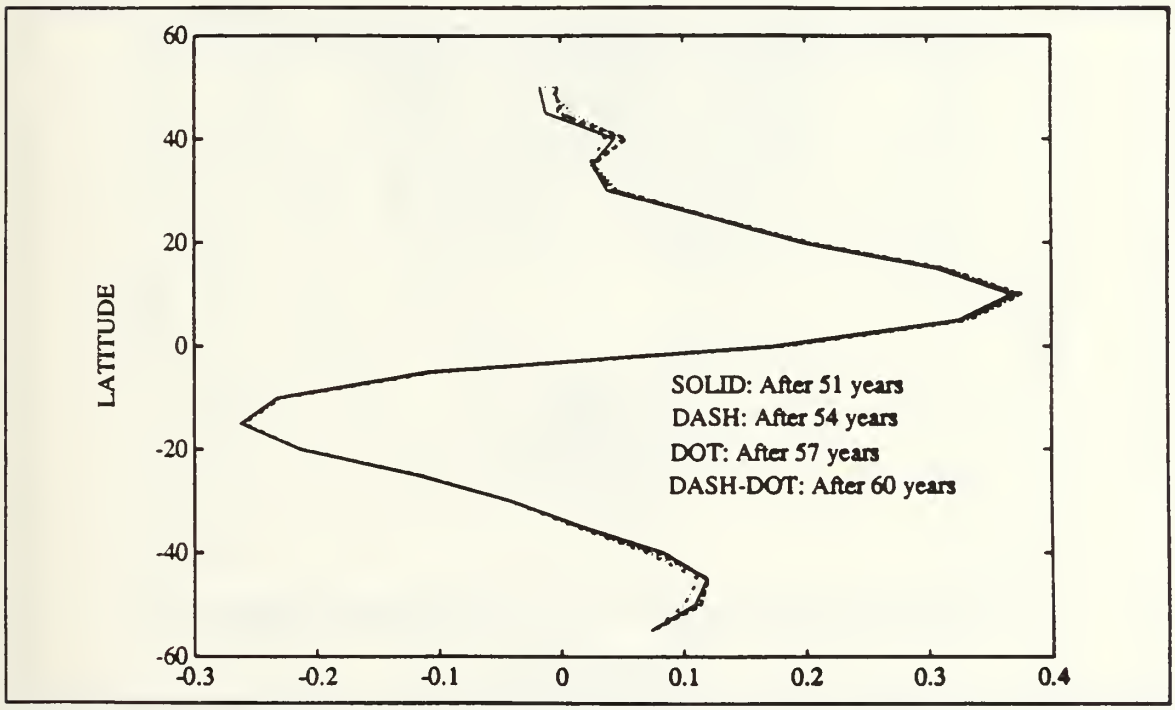

Figure 12. Difference of total northward transport of salt after 51, 54, 57, 60 years integration. ($\times 10^{10}$ cm^3/sec).

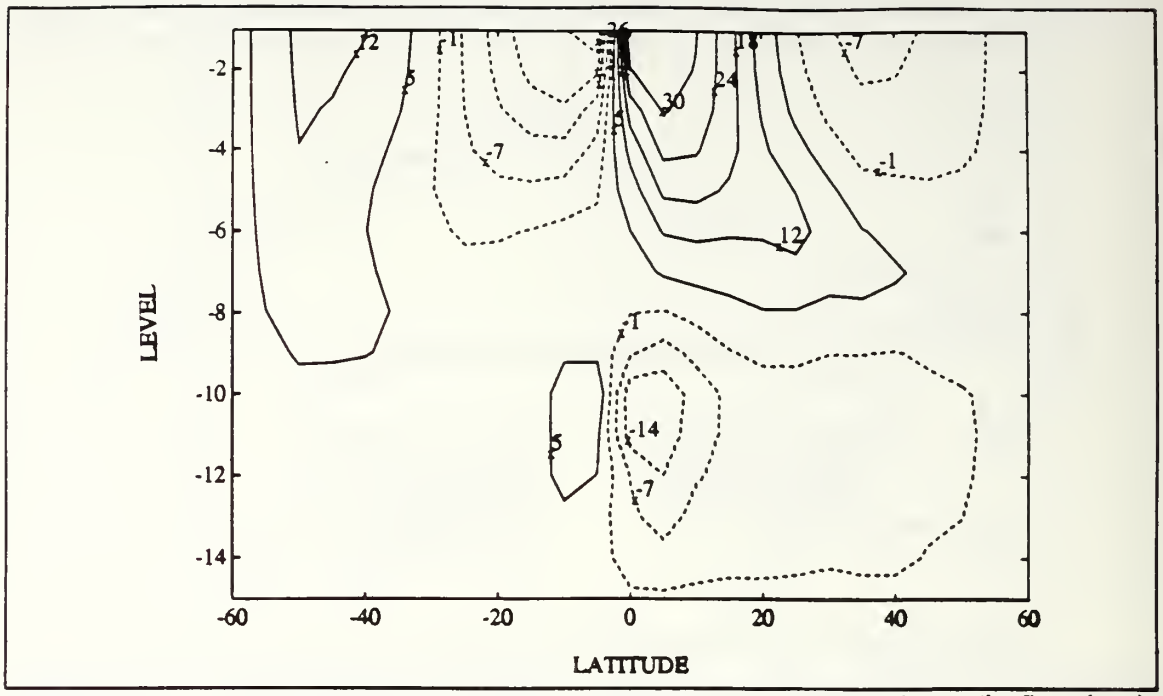

Figure 13. Meridional mass transport after 30 years integration. (in Sverdrup).

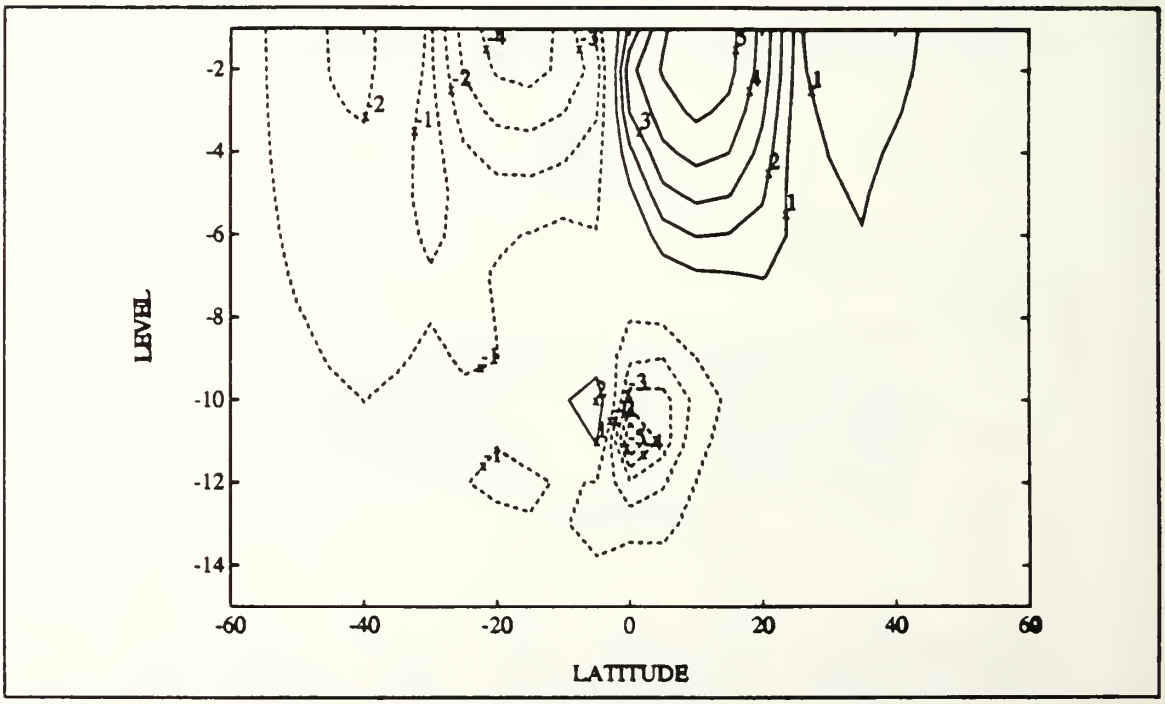

Figure 14. Difference of meridional mass transport after 30 years integration. (in Sverdrup).

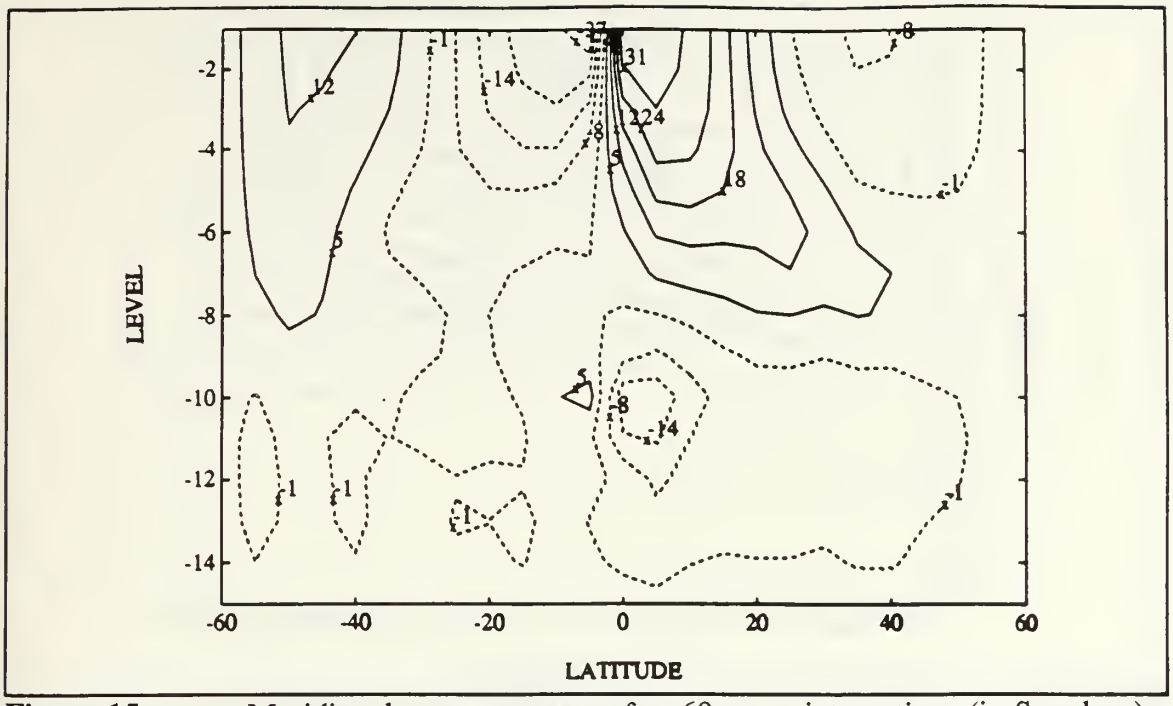

Figure 15. Meridional mass transport after 60 years integration. (in Sverdrup).

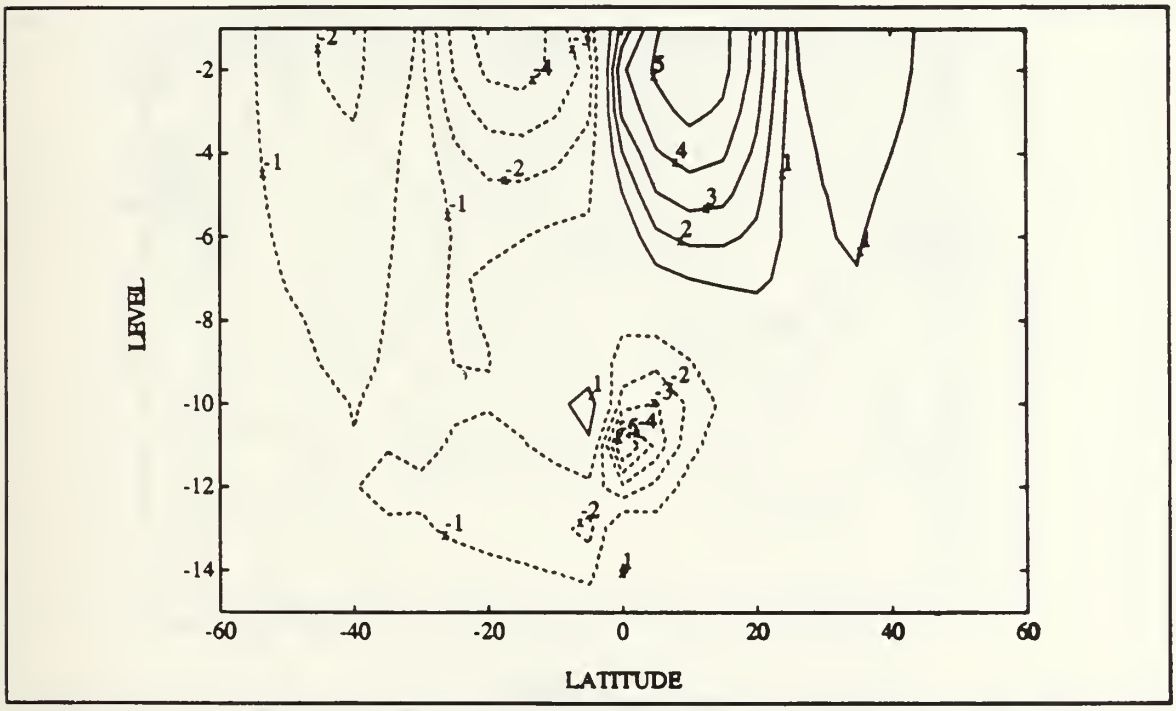

Figure 16. Difference of meridional mass transport after 60 years integration. (in Sverdrup).

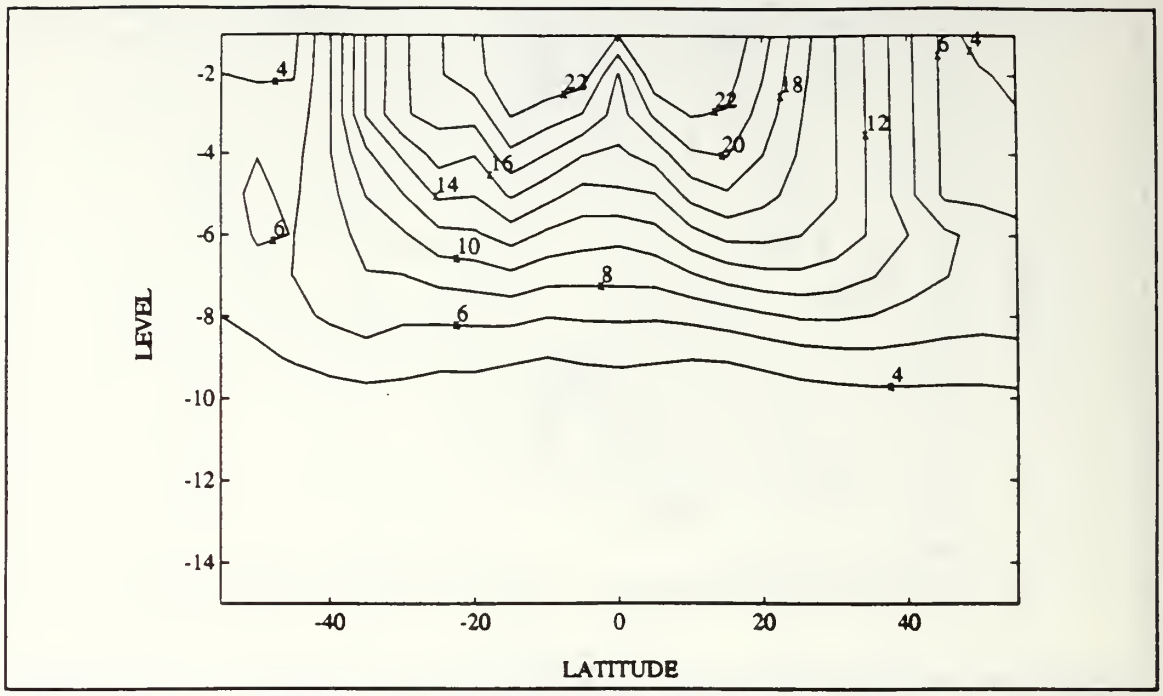

Figure 17. Distribution of temperature (°C) at 160°E meridional section after 60 years integration.

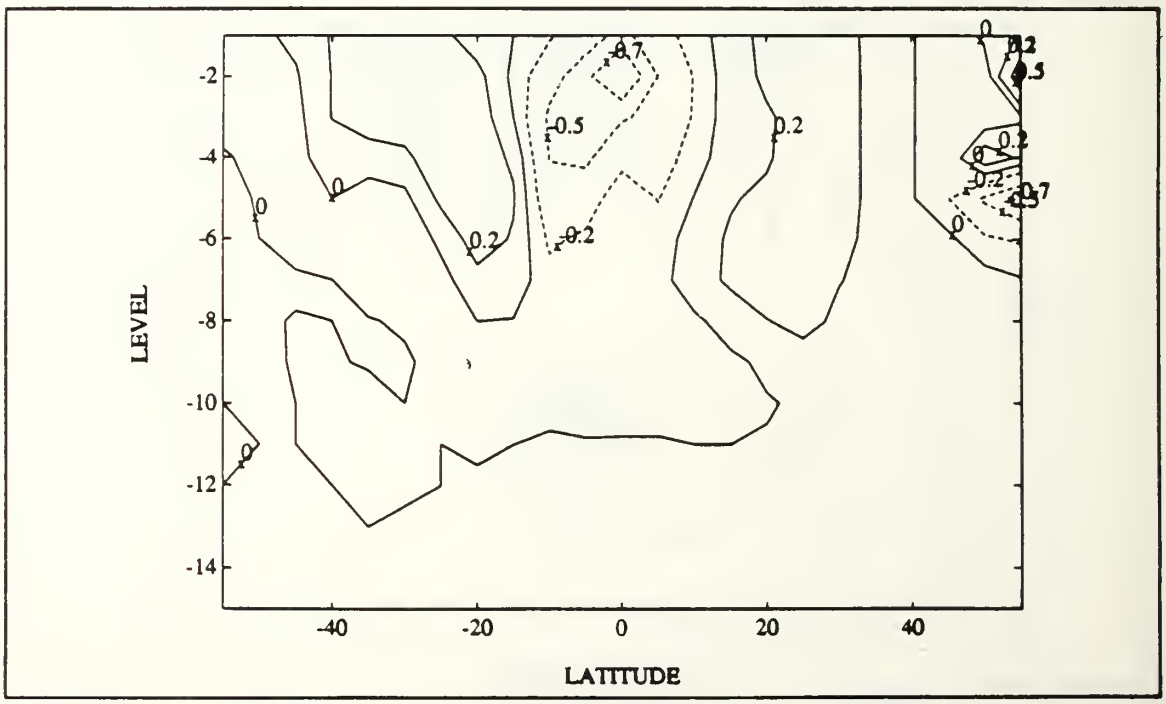

Figure 18. Distribution of temperature difference (°C) at 160°E meridional section after 60 years integration between two different kinds of surface forcing.

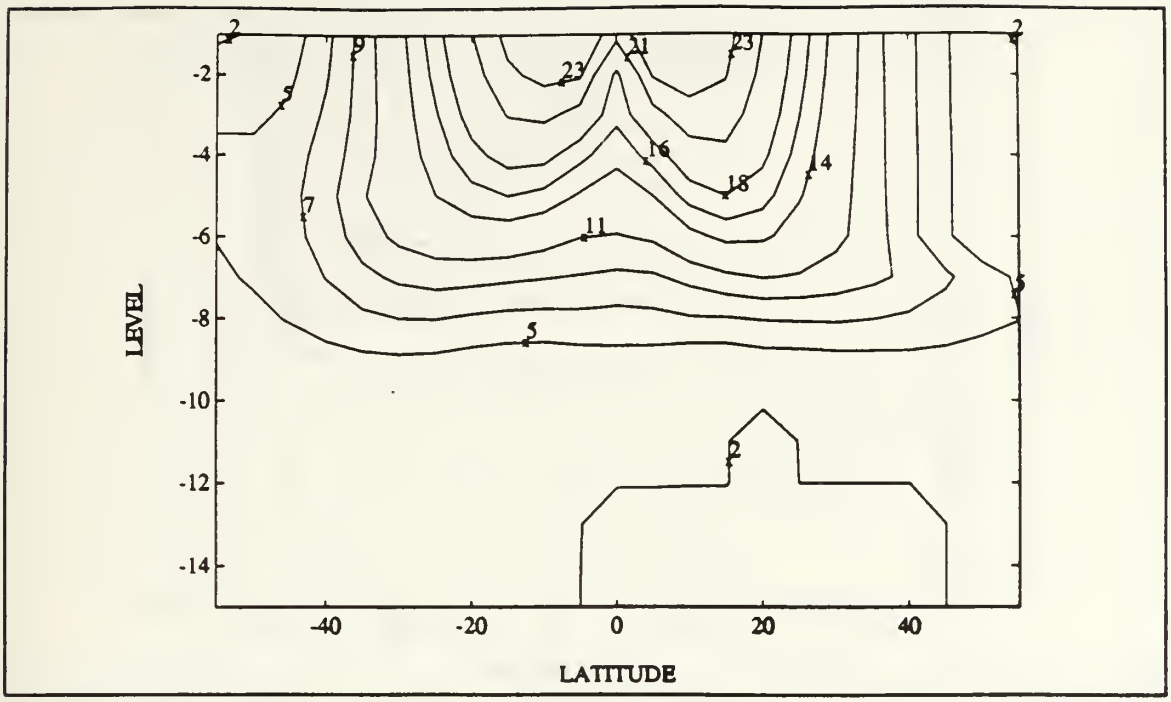

Figure 19. Distribution of temperature (°C) at 160°W meridional section after 60 years integration.

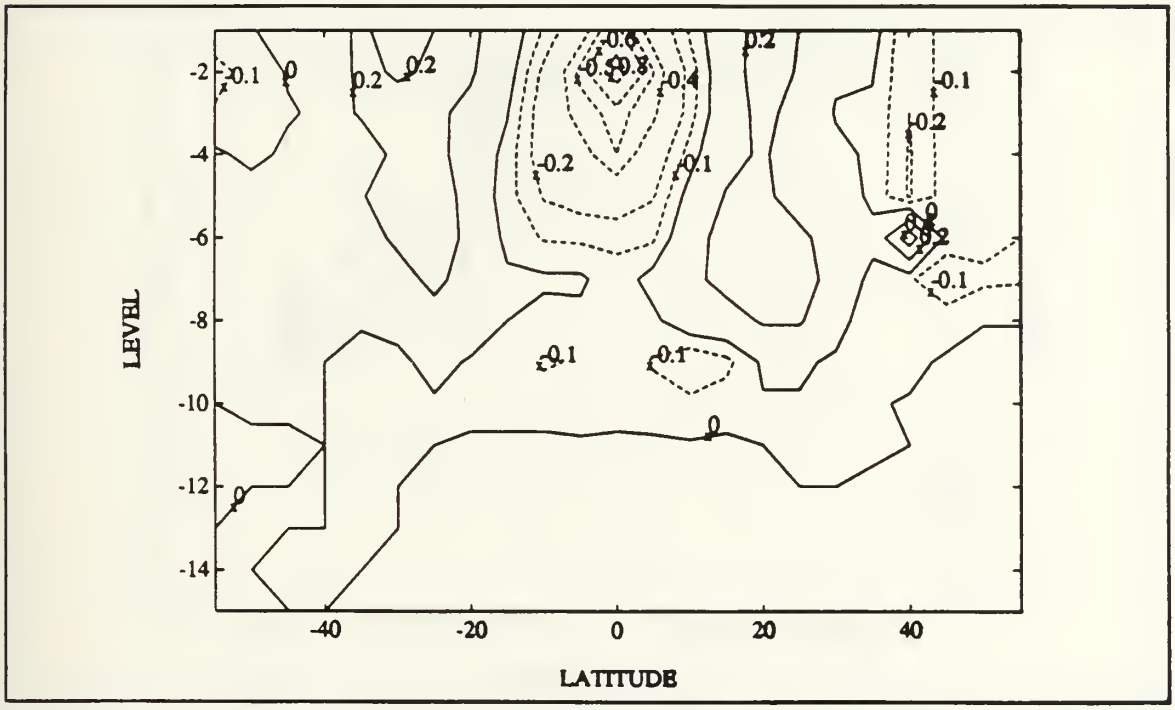

Figure 20. Distribution of temperature difference (°C) at 160°W meridional section after 60 years integration between two different kinds of surface forcing.

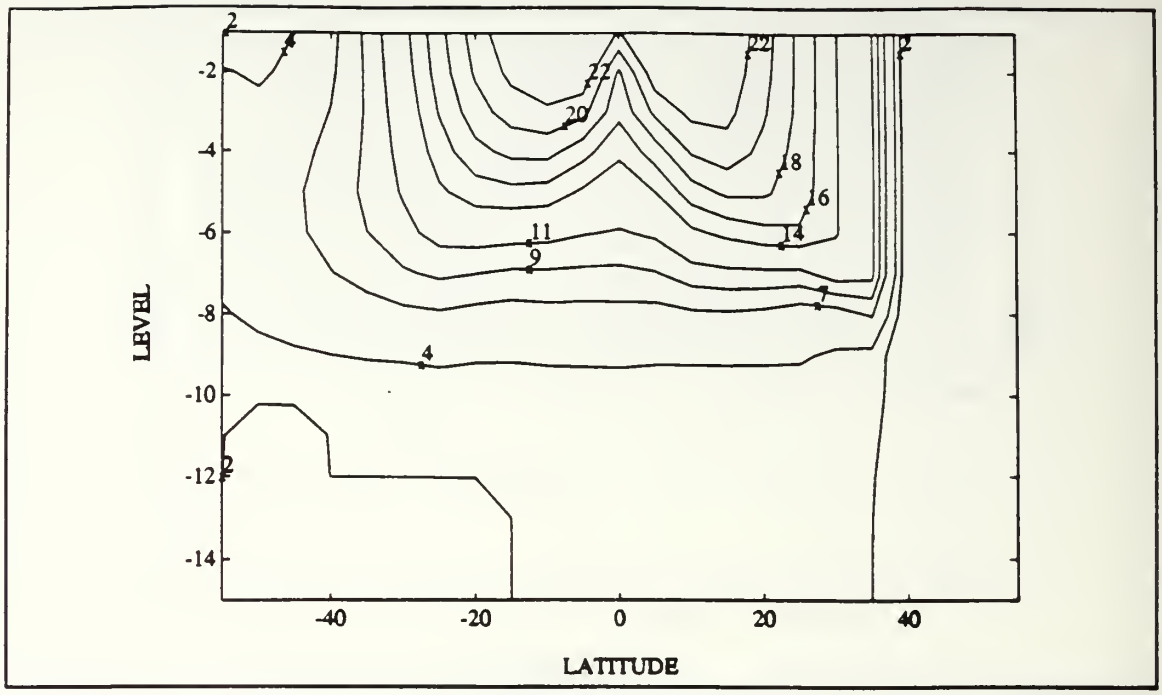

Figure 21. Distribution of temperature (°C) at 120°W meridional section after 60 years integration.

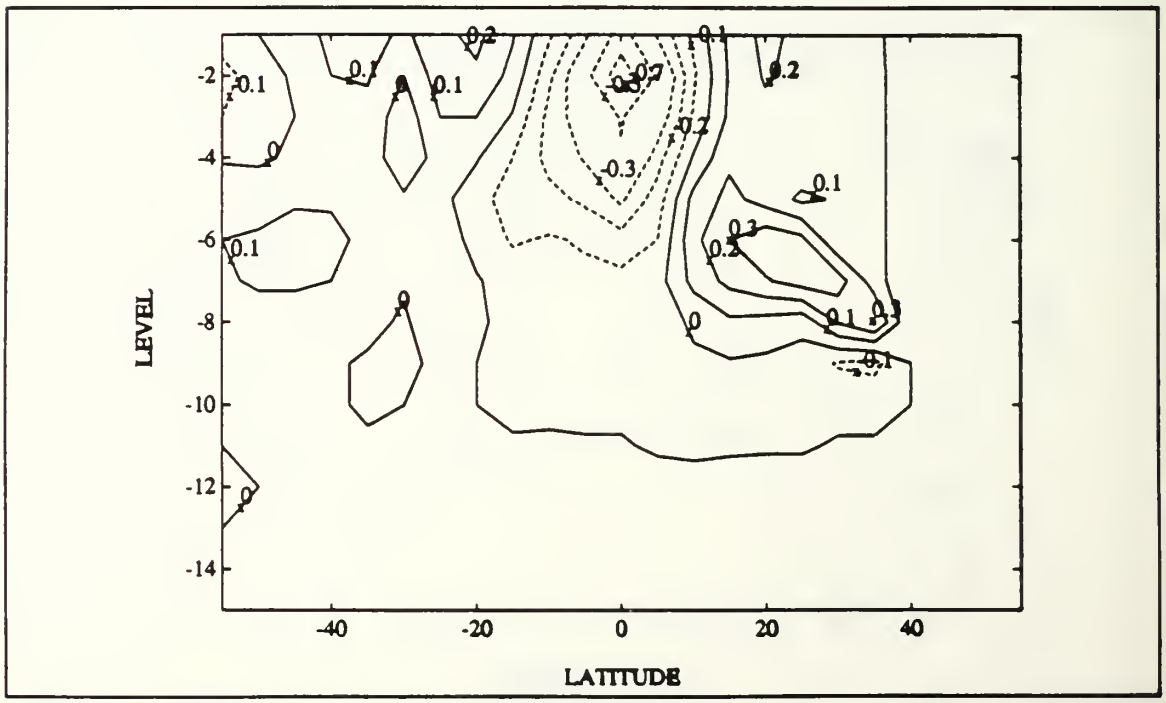

Figure 22. Distribution of temperature difference (°C) at 120°W meridional section after 60 years integration between two different kinds of surface forcing.

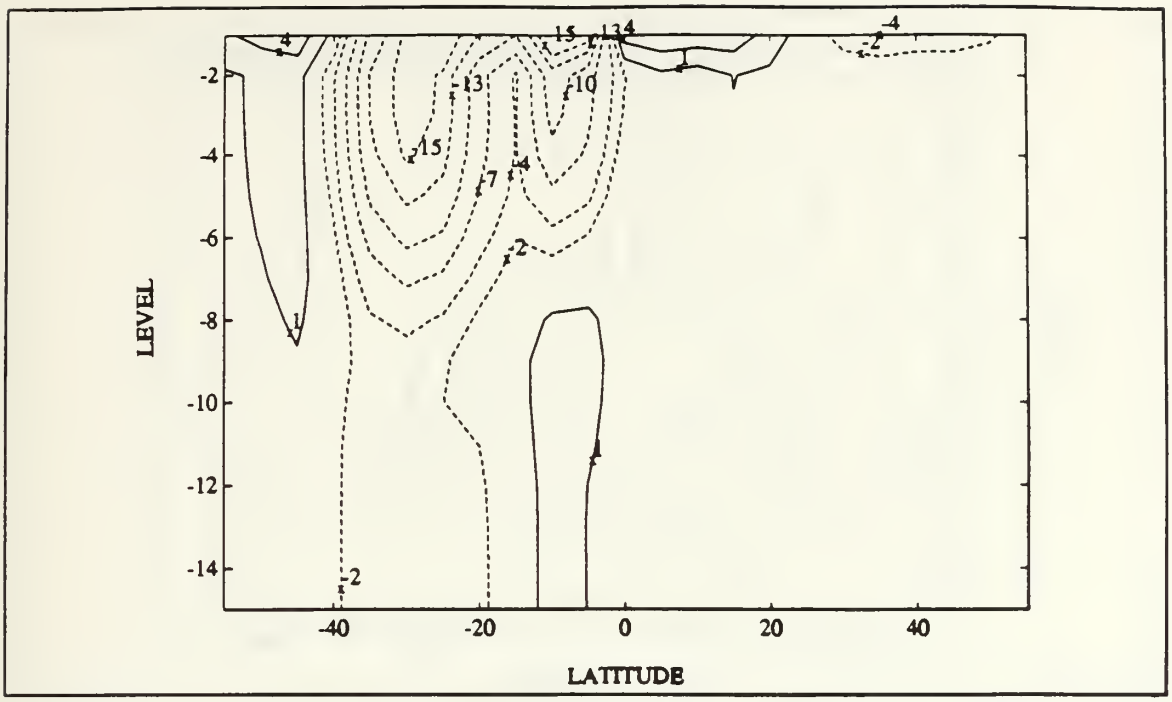

Figure 23. Distribution of v (cm/sec) at 160°E meridional section after 60 years integration.

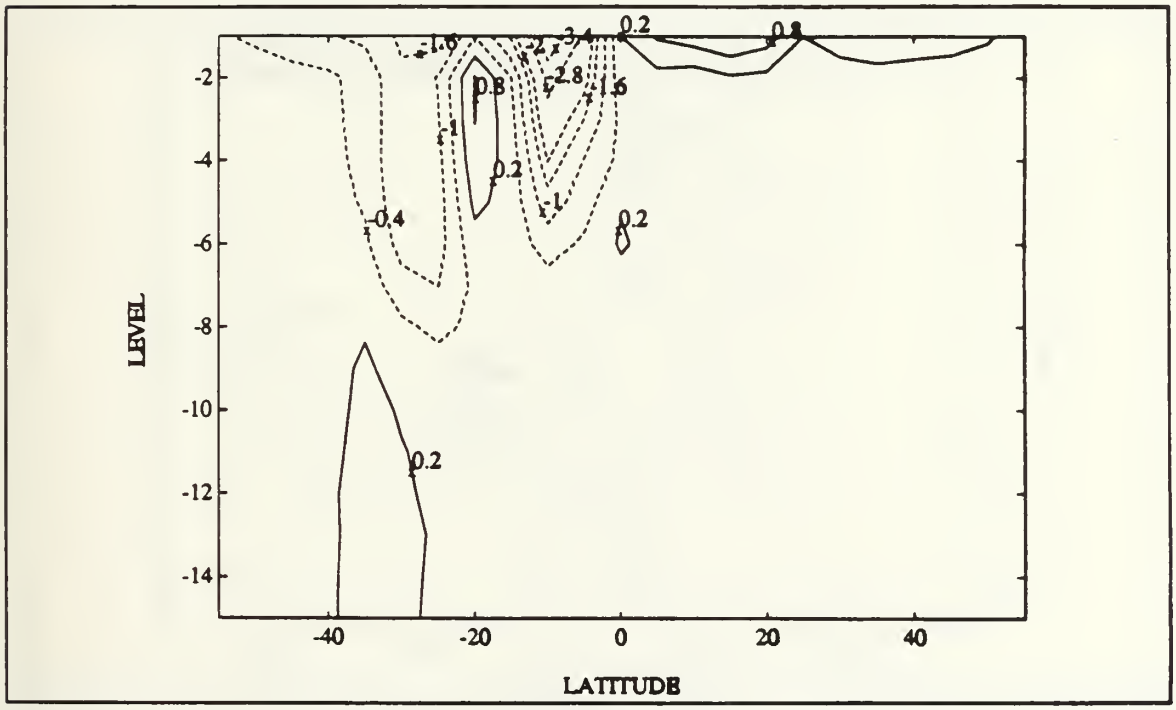

Figure 24. Distribution of v difference (cm/sec) at 160°E meridional section after 60 years integration between two different kinds of surface forcing.

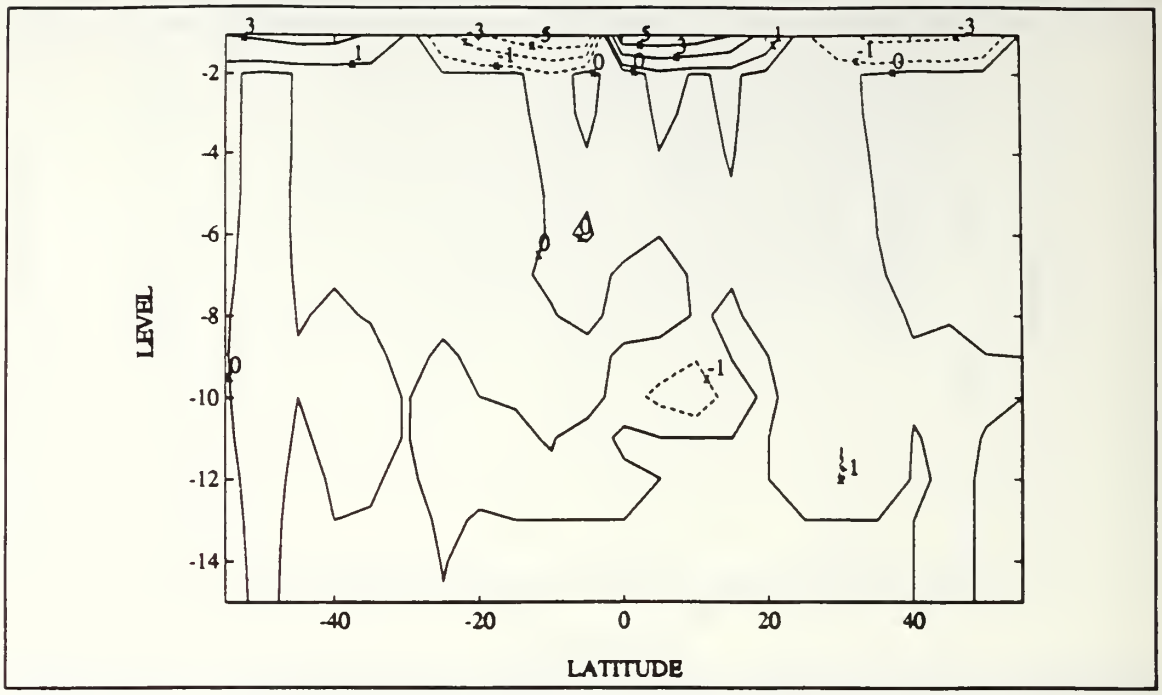

Figure 25. Distribution of v (cm/sec) at 160°W meridional section after 60 years integration.

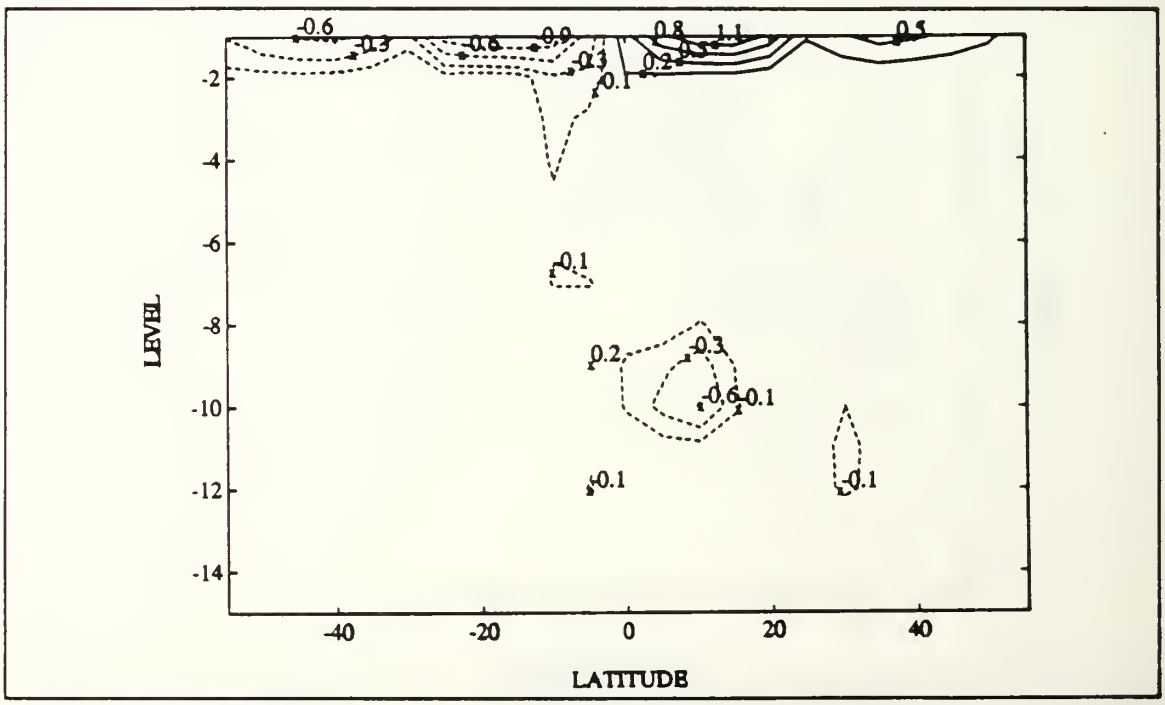

Figure 26. Distribution of v difference (cm/sec) at 160°W meridional section after 60 years integration between two different kinds of surface forcing.

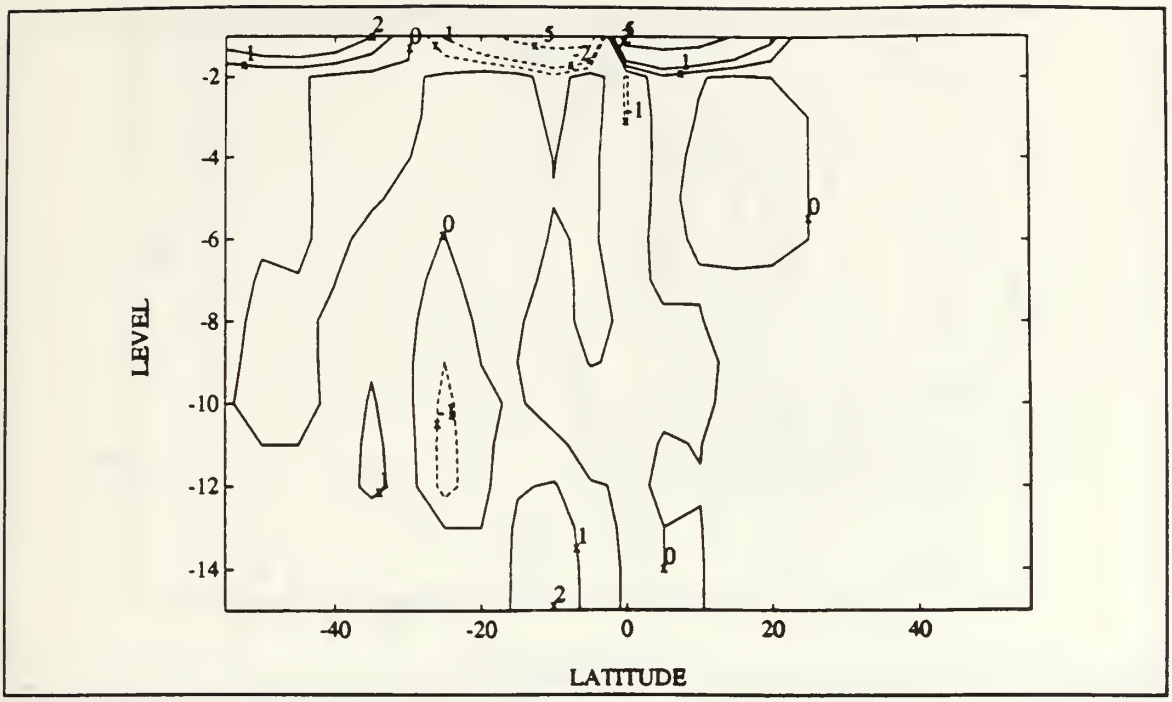

Figure 27. Distribution of v (cm/sec) at 120°W meridional section after 60 years integration.

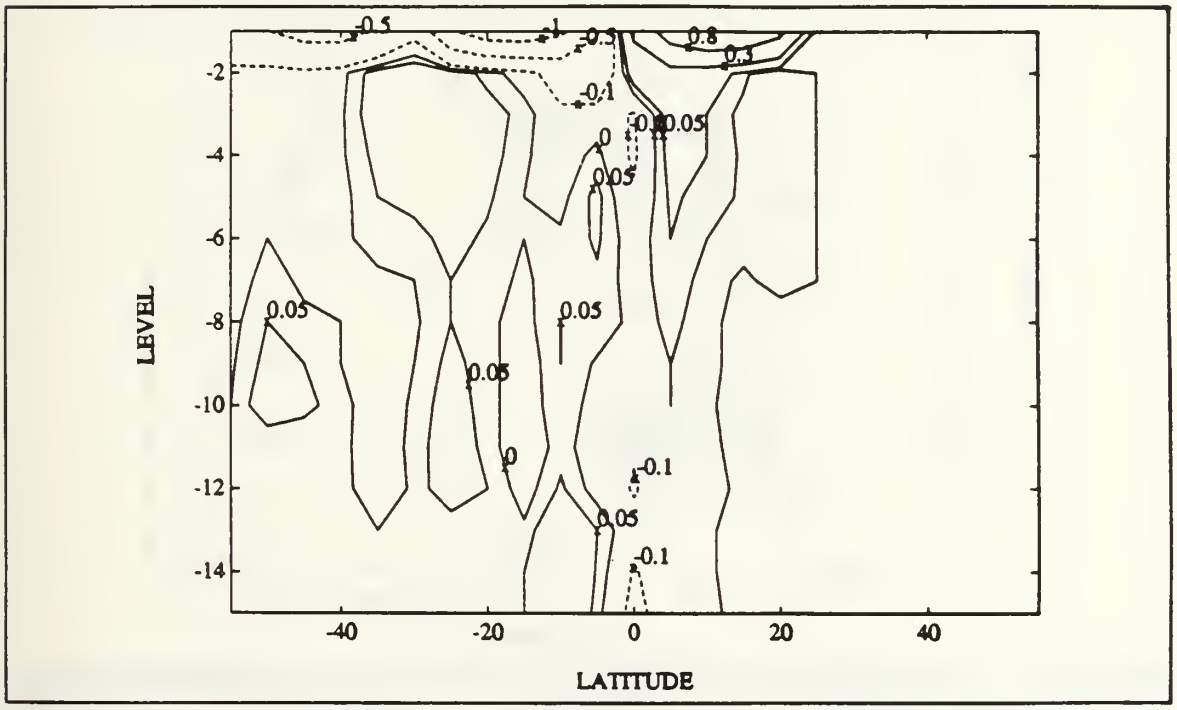

Figure 28. Distribution of v difference (cm/sec) at 120°W meridional section after 60 years integration between two different kinds of surface forcing.

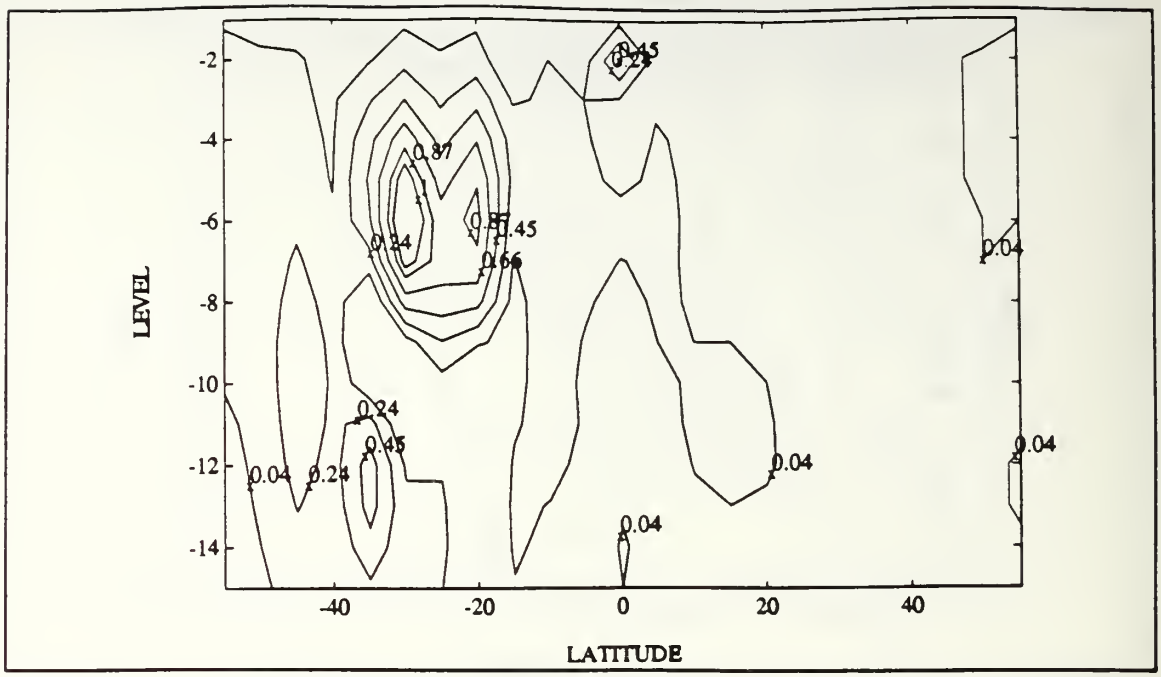

Figure 29. Distribution of w ($\times 10^{-3}$ cm/sec) at 160°E meridional section after 60 years integration.

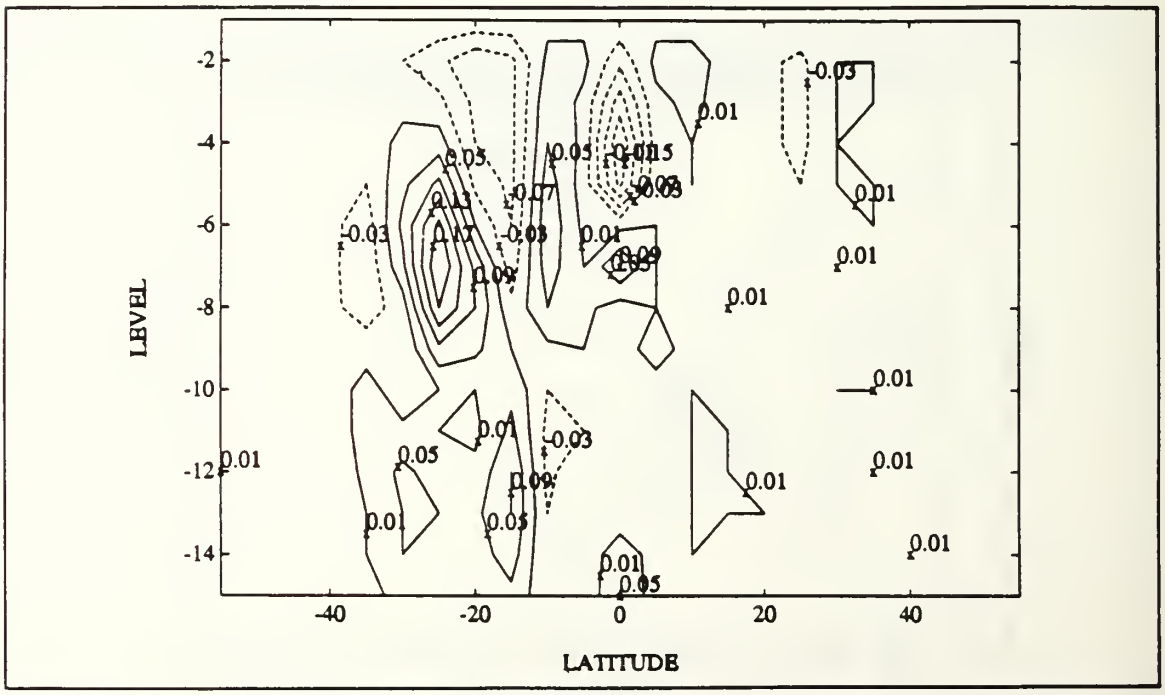

Figure 30. Distribution of w difference ($\times 10^{-3}$ cm/sec) at 160°E meridional section after 60 years integration between two different kinds of surface forcing.

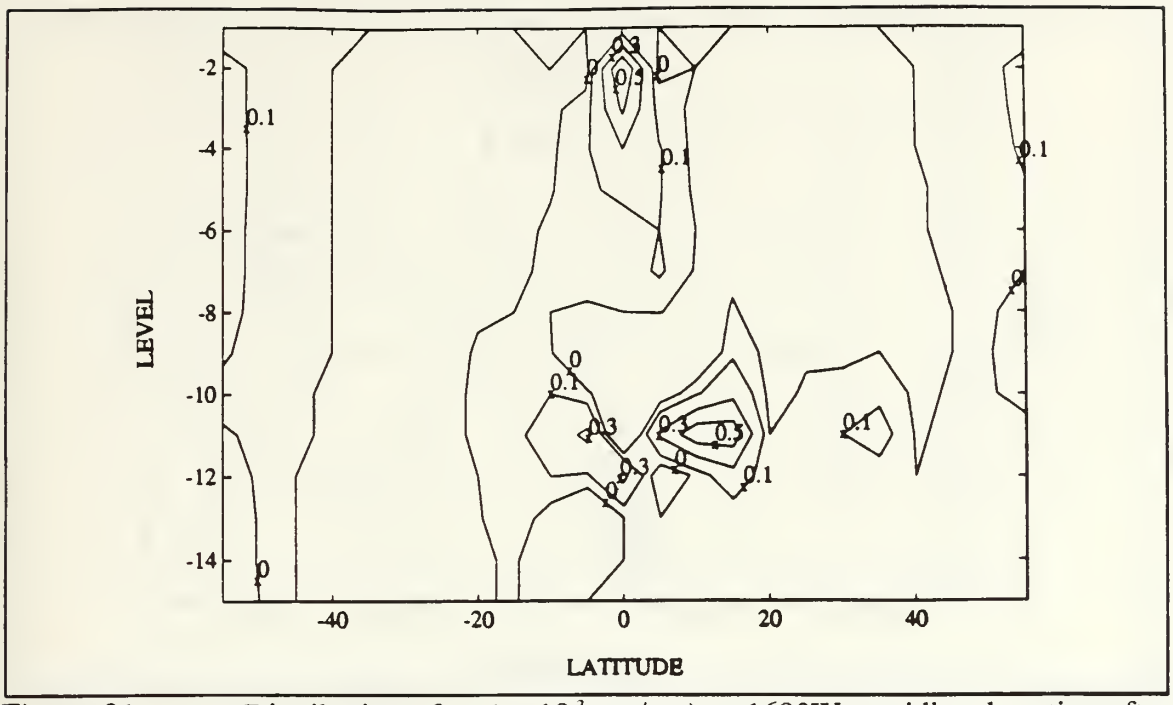

Figure 31. Distribution of w ($\times 10^{-3}$ cm/sec) at 160°W meridional section after 60 years integration.

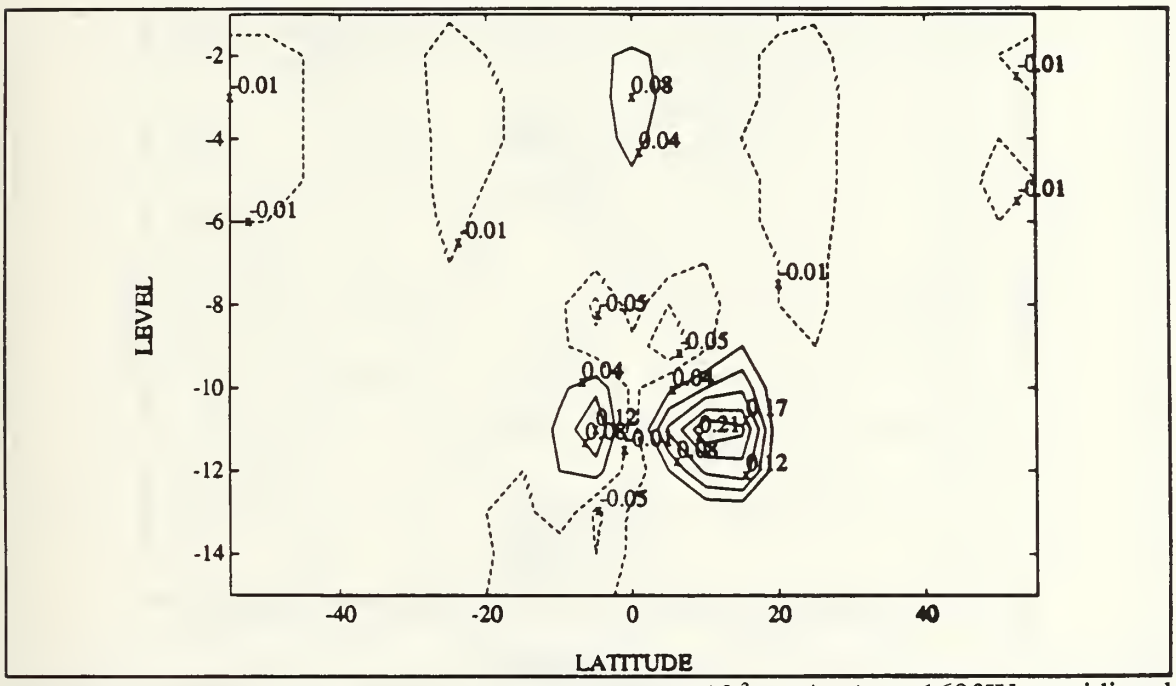

Figure 32. Distribution of w difference ($\times 10^{-3}$ cm/sec) at 160°W meridional section after 60 years integration between two different kinds of surface forcing.

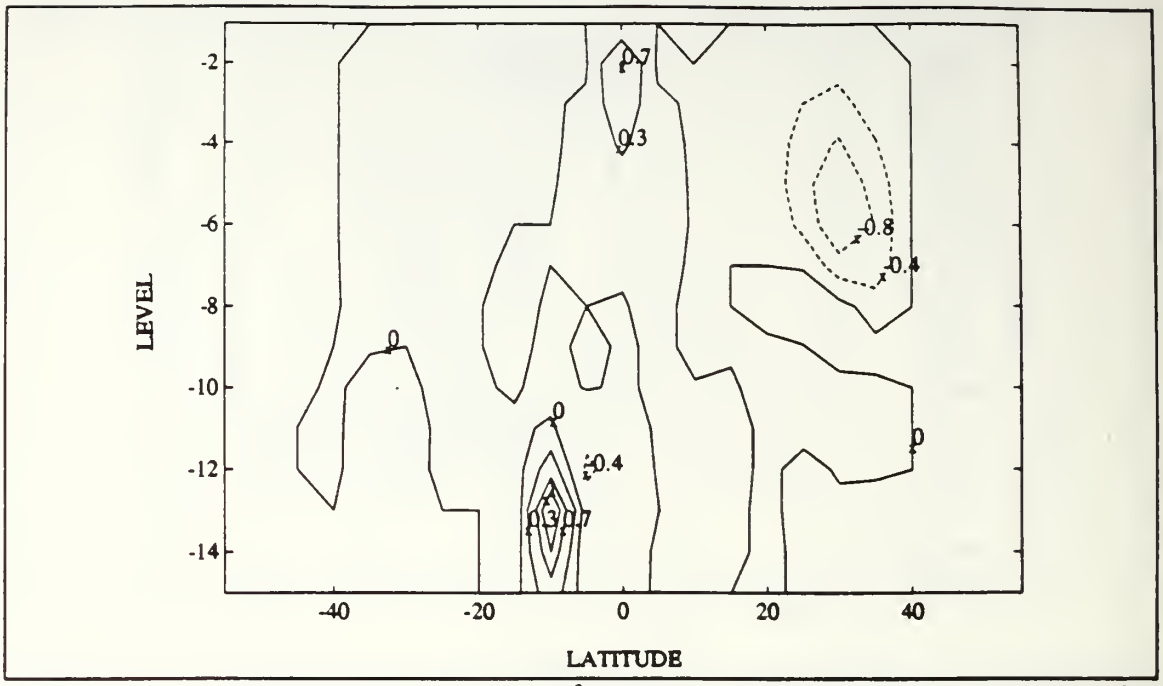

Figure 33. Distribution of w ($\times 10^{-3}$ cm/sec) at 120°W meridional section after 60 years integration.

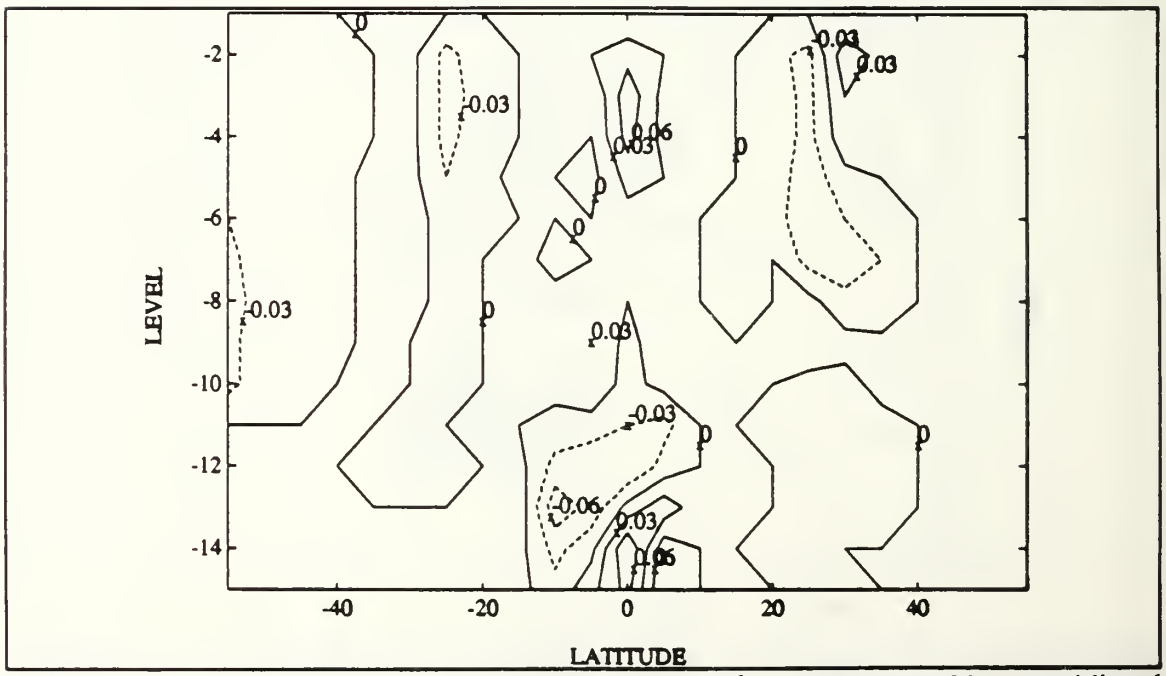

Figure 34. Distribution of w difference ($\times 10^{-3}$ cm/sec) at 120°W meridional section after 60 years integration between two different kinds of surface forcing.

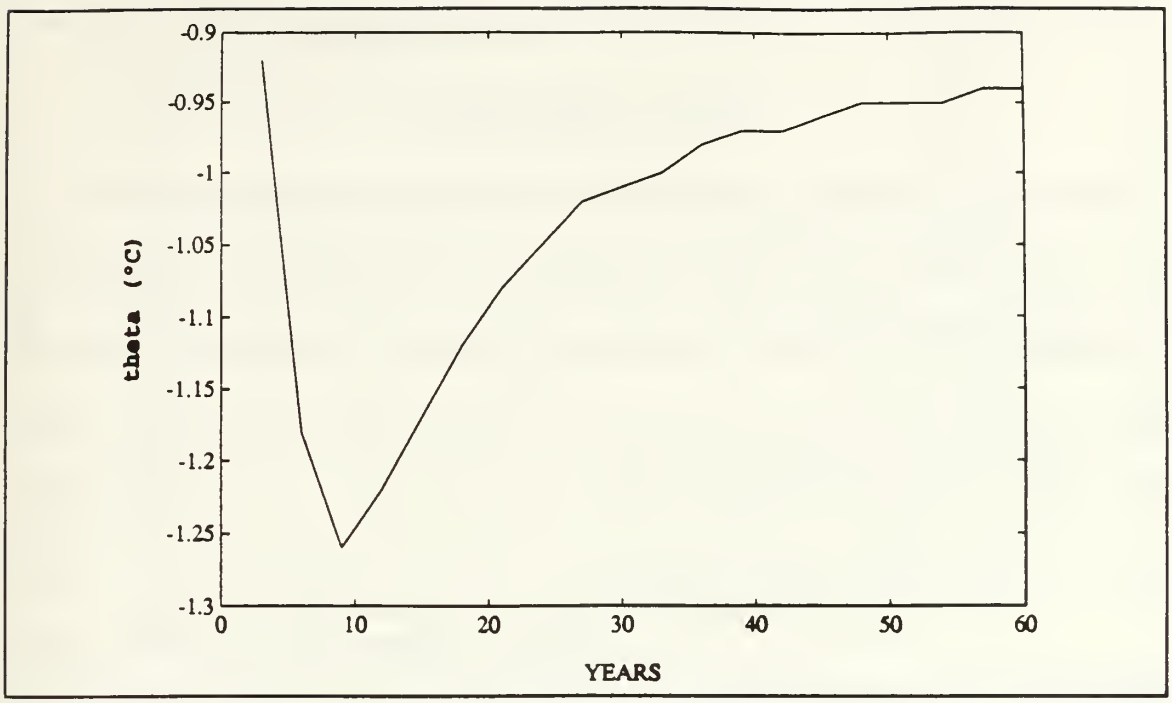

Figure 35. Difference in θ (°C) for depth of 76.15 meters (level 2) at 160°E, 0°N.

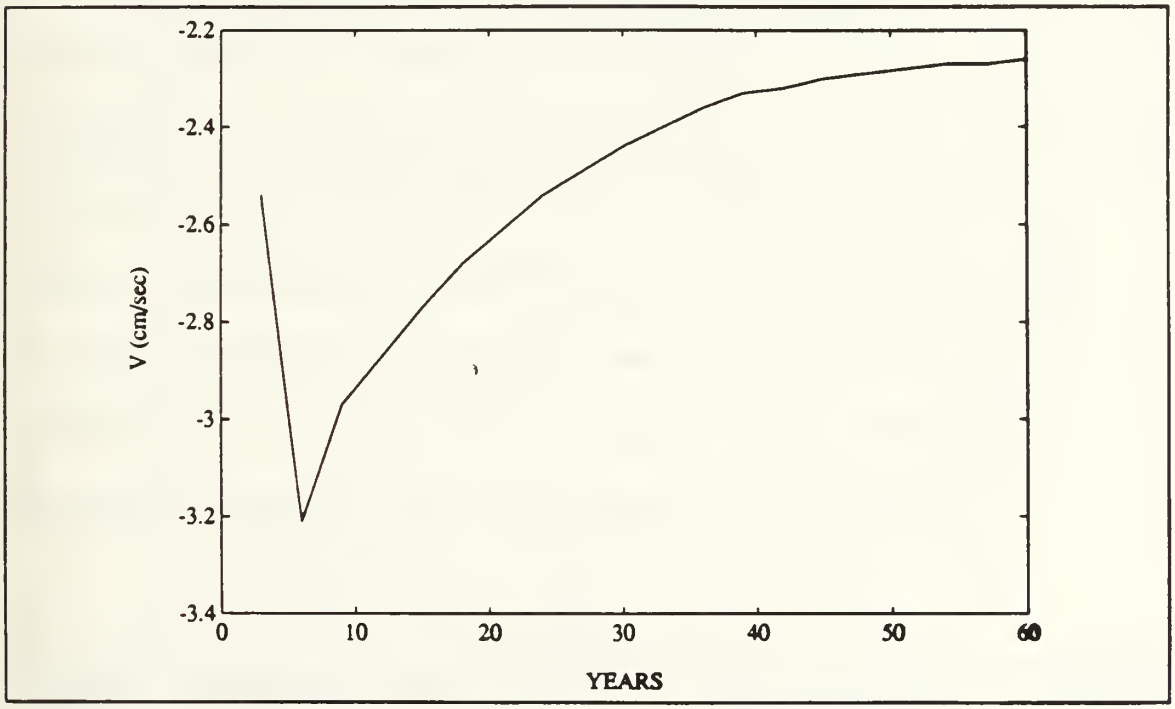

Figure 36. Difference in v (cm/sec) for depth of 76.15 meters (level 2) at 160°E, 5°S.

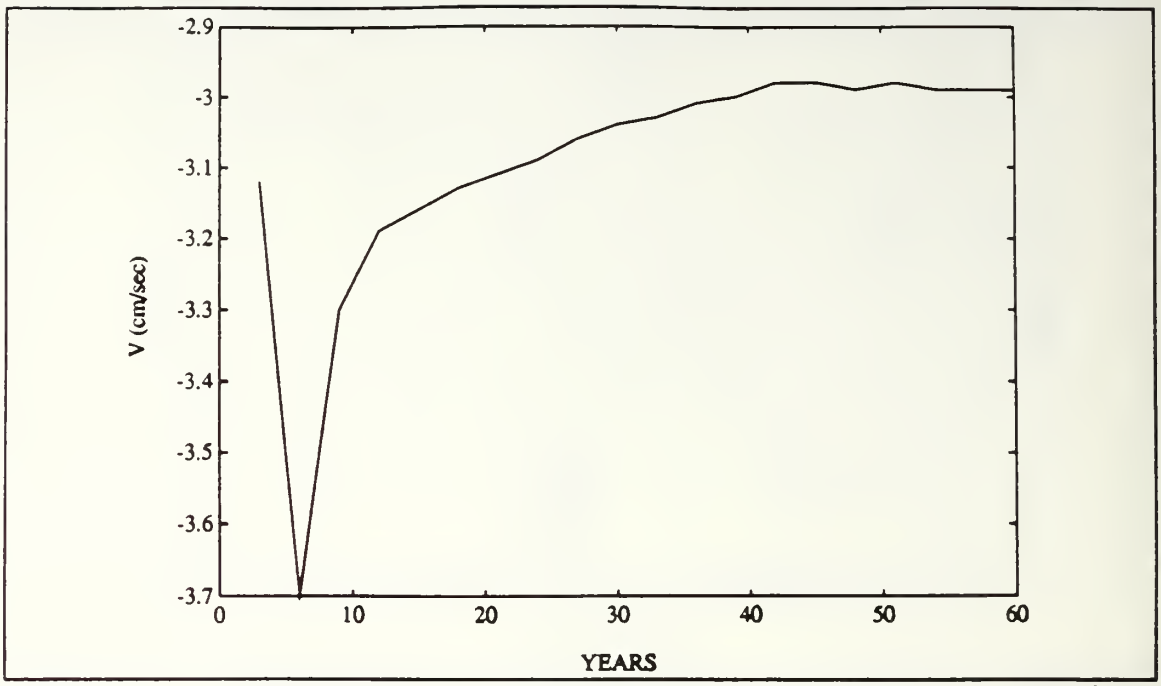

Figure 37. Difference in v (cm/sec) for depth of 76.15 meters (level 2) at 160°E, 10°S.

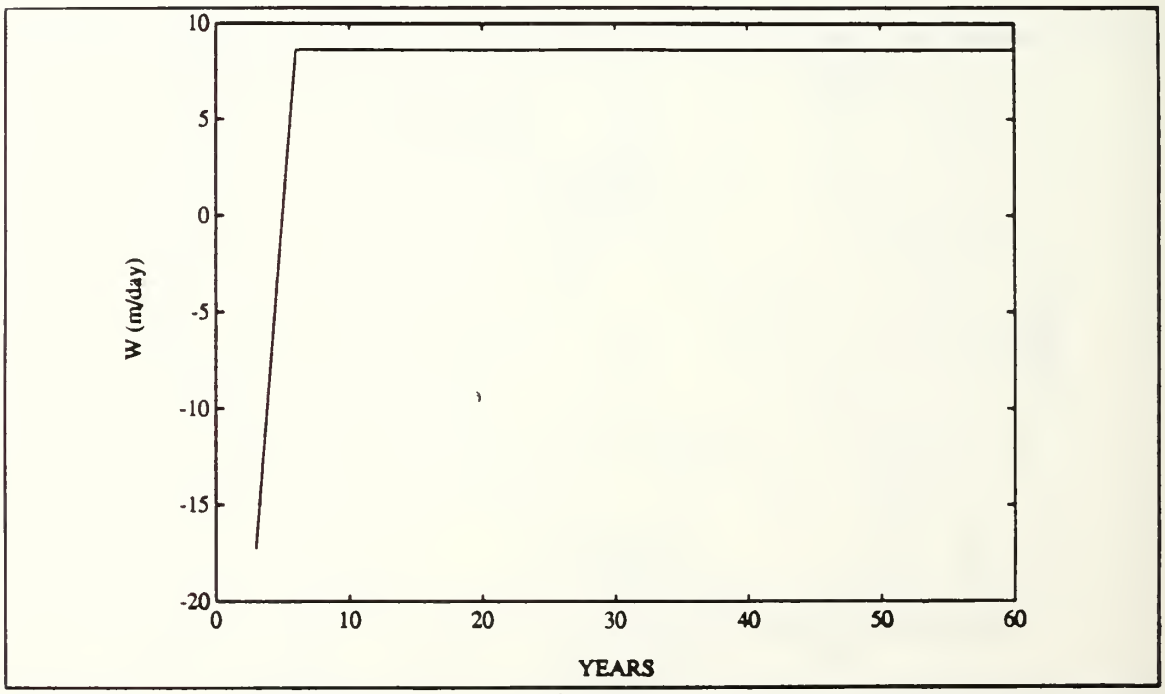

Figure 38. Difference in w ($\times 10^{-3}$ m/day) for depth of 385.64 meters (level 5) at 160°E, 10°N.

V. CONCLUSIONS

The surface wind and surface thermal conditions (e.g., SSAT, net surface heat flux) are important components of the atmospheric system and are related each other. However, the atmospheric parameters representing mechanical and buoyancy forcing, such as surface wind and SST fields (or the net surface heat flux) are often prescribed independently in current ocean models, especially idealized or "process" models. The practice of prescribing wind stress and buoyancy forcing independently in ocean numerical models is an unrealistic assumption.

A large difference between the ocean circulation forced by compatible and incompatible surface forcing (i.e., surface wind stress and buoyancy forcing) has been found by comparing the results from the GFDL MOM model. In particular, the compatible forcing derived from the (incompatible) forcings field of Marotzke and Willebrand (1991), produces 15-20% stronger meridional circulation cells in the low latitudes of both hemispheres of the MOM model. This difference can be attributed to the incompatible SSAT (or surface heat flux) and surface wind fields. Since most ocean numerical models are forced models, a compatible forcing boundary condition is an importance consideration before running any numerical ocean model.

LIST OF REFERENCES

1. Chu, P.C., 1986: An Instability Theory of Ice-air Interaction for the Migration of the Marginal Ice Zone. *Geophys. J. R. Astr. Soc.*, **86,** 863-883.

2. Chu, P.C., 1989: Relationship between Thermally Forced Surface Wind and Sea Surface Temperature Gradient. *Pure Appl. Geophys.*, **130,** 31-45.

3. Chu, P.C., 1992: Incompatible Wind and Buoyancy Forcing in Ocean Numerical Models. *Adv. Atmos. Sci.*, (in press).

4. Bryan, K., and M. D. Cox, 1967: A Numerical Investigation of the Oceanic General Circulation. *Tellus,* **19,** 54-80.

5. Bryan, K., 1969: A Numerical Method for the Study of the Circulation of the World Ocean. *J. Computat. Phys.*, **4,** 347-376.

6. Cox, M.D., 1985: An Eddy Resolving Numerical Model of the Ventilated Thermocline. *J. Phys. Oceanogr.*, **15,** 1312-1324.

7. Cox, M.D., and K. Bryan, 1984: A Numerical Model for Ventilated Thermocline. *J. Phys. Oceanogr.*, **14,** 674-687.

8. Davey, M.K., 1983: A Two-level Model of a Thermally Forced Ocean Basin. *J. Phys. Oceanogr.*, **13,** 169-190.

9. Haney, R.L., 1971: Surface Thermal Boundary Condition for Ocean Circulation Models. *J. Phys. Oceanogr.*, **1,** 241-248.

10. Holton, J.R., 1972: An Introduction to Dynamic Meteorology. Academic Press, New York, 319p.

11. Huang, R.X., 1989: Sensitivity of a Multilayered Ocean General Circulation Model to the Surface Thermal Boundary Condition. *J. Geophys. Res.*, **94,** 18011-18021.

12. Kuo, H.L., 1973: Planetary Boundary Layer Flow of a Stable Atmosphere over the Globe. *J. Atmos. Sci.*, **30,** 53-65.

13. Marotzke, J., and J. Willebrand, 1991: Multiple Equilibria of the Global Thermohaline Circulation. *J. Phys. Oceanogr.*, **21,** 1372-1385.

14. Robinson, A.R., D.E. Harrison, Y. Mintz, and A.J. Semtner, Jr., 1977: Eddies and the General Circulation of an Idealized Oceanic gyre: a Wind and Thermally Driven Primitive Equation Numerical Experiment. *J. Phys. Oceanogr.*, **7**, 182-207.

15. Semtner, A.J., Jr., and Y. Mintz, 1977: Numerical Simulation of the Gulf Stream and Mid-ocean Eddies. *J. Phys. Oceanogr.*, **7**, 208-230.

16. Takano, K., 1975: A Numerical Simulation of the World Ocean Circulation: Preliminary Results. In: *Numerical Models of Ocean Circulation.* National Academy of Sciences, Washington D.C., 121-129.

17. Willmont, A.J., and M.S. Darby: Nonlinear Rossby Waves in a Thermodynamic Reduced Gravity Ocean. *Geophys. Astrophys. Fluid Dyn.*, **54**, 189-227.

INITIAL DISTRIBUTION LIST

1.	Defense Technical Information Center Cameron Station Alexandria, VA 22304-6145	2
2.	Dudley Knox Library Code 0142 Naval Postgraduate School Monterey, CA 93943-5002	2
3.	Chairman Dr. Robert L. Haney Code MR/Hy Department of Meteorology Naval Postgraduate School Monterey, CA 93943	1
4.	Professor Peter C. Chu Code OC/Cu Department of Oceanography Naval Postgraduate School Monterey, CA 93943	2
5.	LT Kuo, Yu-Heng NO. 17-3, Ping-Shan Hsin Tsun, Tsoying, Kaohsiung, Taiwan, R. O. C.	6
6.	Naval Academy Library P.O. Box 90175 Tsoying, Kaohsiung, Taiwan, R. O. C.	2